



**US Army Corps
of Engineers**
Waterways Experiment
Station

AD-A286 422



Technical Report ITL-94-7
September 1994

①

In-House Laboratory Independent Research Program

Application of Computational and Visualization Methods to Groundwater Modeling

by Fred T. Tracy

40

94-35628



NOV 21 1994

[illegible]

Approved For Public Release; Distribution Is Unlimited

Plaintiff will be in black and
some will be in blue and
some will be in white.

Prepared for Assistant Secretary of the Army (R&D)

Loosenen Vor

1

7



Abstract

100

1

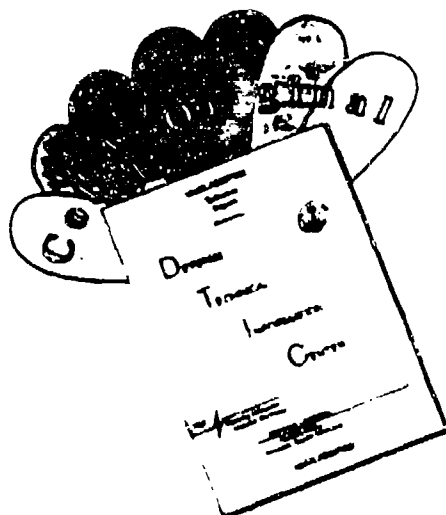
Abstract

1



PRINTED ON RECYCLED PAPER

DISCLAIMER NOTICE



THIS DOCUMENT IS BEST QUALITY AVAILABLE. THE COPY FURNISHED TO DTIC CONTAINED A SIGNIFICANT NUMBER OF COLOR PAGES WHICH DO NOT REPRODUCE LEGIBLY ON BLACK AND WHITE MICROFICHE.

**In-House Laboratory Independent
Research Program**

Technical Report ITL-94-7
September 1994

Application of Computational and Visualization Methods to Groundwater Modeling

by Fred T. Tracy

U.S. Army Corps of Engineers
Waterways Experiment Station
3909 Halls Ferry Road
Vicksburg, MS 39180-6199

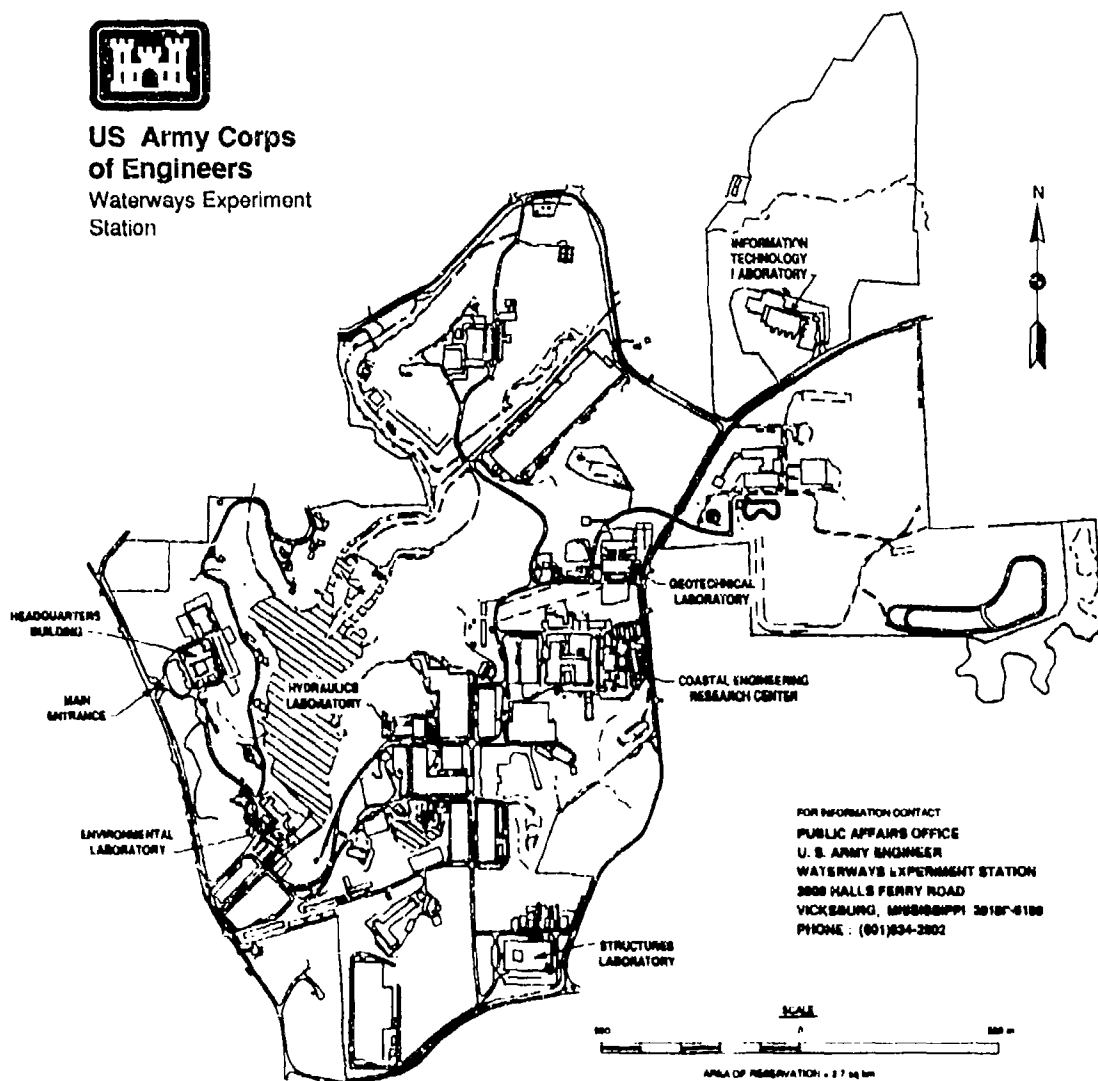
Final report

Approved for public release; distribution is unlimited

Prepared for Assistant Secretary of the Army (R&D)
Washington, DC 20315



**US Army Corps
of Engineers**
Waterways Experiment
Station



FOR INFORMATION CONTACT
PUBLIC AFFAIRS OFFICE
U. S. ARMY ENGINEER
WATERWAYS EXPERIMENT STATION
3808 HALLS FERRY ROAD
VICKSBURG, MISSISSIPPI 39182-6100
PHONE : (601) 634-2802

Waterways Experiment Station Cataloging-in-Publication Data

Tracy, Fred T.

Application of computational and visualization methods to groundwater modeling / by Fred T. Tracy ; prepared for Assistant Secretary of the Army (R&D).

68 p. : ill. ; 28 cm. — (Technical report ; ITL-94-7)

Includes bibliographic references.

1. Diffusion in hydrology — Mathematical models. 2. Groundwater flow — Colorado — Rocky Mountain Arsenal Region — Data processing. 3. Finite element method — Data processing. 4. Color computer graphics. I. United States. Army. Corps of Engineers. II. U. S. Army Engineer Waterways Experiment Station. III. Information Technology Laboratory (US Army Corps of Engineers, Waterways Experiment Station) IV. In-house Laboratory Independent Research Program (U. S. Army Engineer Waterways Experiment Station) V. United States. Assistant Secretary of the Army (Research, Development, and Acquisition) VI. Title. VII. Series: Technical report (U. S. Army Engineer Waterways Experiment Station) ; ITL-94-7.

TA7 W34 no.ITL-94-7

Contents

| | |
|--|----|
| Preface | v |
| 1—Introduction | 1 |
| Why This Research? | 1 |
| Cray Y-MP | 1 |
| Scientific Visualization | 1 |
| Chapter Summaries | 2 |
| 2—Saturated Flow | 3 |
| Introduction | 3 |
| Description of Problem | 4 |
| 2-D Results | 8 |
| 3-D Study | 9 |
| 3-D grid | 9 |
| 3-D groundwater model | 12 |
| Visualization of 3-D results | 13 |
| Cray Y-MP improvements | 16 |
| Solution process | 17 |
| I/O | 18 |
| 2-D Versus 3-D Comparison | 18 |
| Grid Display | 20 |
| Summary and Conclusions | 20 |
| 3—Unsaturated Flow | 26 |
| Introduction | 26 |
| Governing Equations | 26 |
| (x, y, z) equations | 26 |
| (ξ , η , ζ) equations | 27 |
| Computational Procedure | 30 |
| Finite volume cell | 30 |
| Discretized equation | 31 |
| Computation of geometric quantities | 33 |
| Nonlinear iteration | 35 |
| Test Problems | 36 |
| Dupuit's problem | 36 |
| Laboratory test problem | 38 |
| Summary and Conclusions | 42 |

| | |
|--|----|
| 4—Contaminant Transport | 43 |
| Introduction | 43 |
| Governing Equations | 43 |
| Eulerian Versus Lagrangian Approach | 45 |
| Computational Procedure | 46 |
| Langrangian step | 46 |
| Eulerian step | 49 |
| Test Problems | 50 |
| 1-D steady-state transport | 50 |
| 2-D transient transport | 50 |
| Scientific Visualization | 54 |
| Summary and Conclusions | 55 |
| References | 56 |
| Appendix A: Derivation of Curvilinear Coordinate Equations | A1 |
| Purpose | A1 |
| Coordinate System | A1 |
| Geometric Conservation Law | A2 |
| Gradient | A3 |
| Divergence | A3 |

SF 298

Preface

This report describes research into several areas of groundwater modeling. The primary focus of this work is basic research on computational algorithms, but a secondary aspect is a study of the use of scientific visualization technology. The work was funded under the In-House Laboratory Independent Research (ILIR) program at the U.S. Army Engineer Waterways Experiment Station (WES), Vicksburg, MS. Additional research and the publication of this report were funded by the Strategic Environmental Research and Development Program (SERDP), Department of Defense.

Dr. James H. May and CPT Edward Mazion, Engineering Geology Branch, Earthquake Engineering and Geophysics Division, Geotechnical Laboratory (GL), WES, performed the 2-D Rocky Mountain Arsenal (PMA) study described in this report. Mr. John B. Palmerton, Rock Mechanics Branch, Soil and Rock Mechanics Division, GL, WES, performed the analysis of Cerrillos Dam in Puerto Rico discussed in this report. Most of the scientific visualization work for RMA was done by Mr. Scott Weberg, Scientific Visualization Center (SVC), Advanced Technology Center (ATC), Information Management Division (IMD), Information Technology Laboratory (ITL), WES. Mr. Charles S. Jones, SVC, ATC, IMD, ITL, WES, assisted in the visualization for contaminant transport. Cray Y-MP improvements were made by Mr. Alex Carrillo, Department of Defense High Performance Computing Center, ATC, IMD, ITL, WES. Dr. Fred T. Tracy, Interdisciplinary Research Group, Computer-Aided Engineering Division (CAED), ITL, WES, wrote this report (Mr. Carrillo provided an excellent draft documenting his work) and performed the remaining work described herein. Dr. Reed L. Mosher was Acting Chief of CAED during this study and preparation of this report, and Director of ITL was Dr. N. Radhakrishnan.

This work was coordinated with the WES Groundwater Modeling Team whose chairman is Dr. Jeffery P. Holland, Director, Computational Hydraulics Institute, Hydraulics Laboratory, and Program Manager, Groundwater Modeling Program.

At the time of publication of this report, Director of WES was
Dr. Robert W. Whalin. Commander was COL Bruce K. Howard, EN.

*The contents of this report are not to be used for advertising, publication,
or promotional purposes. Citation of trade names does not constitute an
official endorsement or approval of the use of such commercial products.*

1 Introduction

Why This Research?

The flow of groundwater is an extremely complex process to model because of the diverse types of flow and the heterogeneous nature of the porous media. When the transport of diverse types of contaminants is added to the problem, the difficulty and complexity of modeling real-world three-dimensional (3-D) groundwater flow increases by orders of magnitude. Also, it is very difficult to visualize groundwater input and output into numerical programs because of the complexity of the geometry and heterogeneity of the porous medium. This report documents basic and applied research in the area of groundwater modeling and visualization.

Cray Y-MP

The use of a supercomputer such as a Cray Y-MP is also essential for the timely computation of results of a large 3-D groundwater model. This is because the highly nonlinear nature of the soil properties in the unsaturated zone creates a tremendous computational load, and traditional techniques do several iterations at each time-step in an attempt to achieve suitable answers. Further complications arise because groundwater flow is sometimes modeled over extremely long periods of time, putting an additional requirement that the numerics remain stable and robust. This report describes research findings in this area as well.

Scientific Visualization

The use of graphical tools to visualize both the input data (grid with initial and boundary conditions) and the results (pressure, head, velocity, concentration, etc.) is absolutely essential for successful modeling. This report also describes the scientific visualization techniques developed in this research.

Chapter Summaries

Chapter 2 uses the application of the real-world problem of flow near Rocky Mountain Arsenal (RMA) to help answer the question of when a 3-D analysis is needed. A comparison of a two-dimensional (2-D) plan view time-dependent solution taken to steady state to a true 3-D saturated flow solution where the phreatic surface is iterated to the steady-state solution is presented. Both these solutions use the finite element method (FEM). The details of what was done to create the 3-D FEM program and data are given. Examples of how visualization was used are also given.

The running times for the 3-D saturated flow steady-state RMA problem using classical FEM solution techniques showed that for 3-D, time-dependent, nonlinear problems involving unsaturated or multiphase flow with contaminant transport, the running times even on the Cray Y-MP could possibly become prohibitive. Therefore, Chapters 3 and 4 describe basic research into other techniques that are potentially faster and, for those problems where they can be applied, should deliver an equivalent quality answer much more efficiently. Specifically, the finite volume (FV) method is first applied to saturated/unsaturated flow and then to contaminant transport and compared to classical FEM solutions. The techniques of nonlinear iteration, operator splitting, etc., are also discussed. Both experimental results and analytical solutions are used to compare different procedures. Finally, contaminant transport results are viewed using scientific visualization tools.

2 Saturated Flow

Introduction

Engineers and scientists at the Geotechnical Laboratory (GL), U.S. Army Engineer Waterways Experiment Station (WES), have made a study of flow in the RMA region. The program used for the study is a modified version of a 2-D plan view saturated and confined flow FEM code (Warner 1987) that accepts a triangular grid. This report describes three additional things that were done as follows:

- a. *Three-dimensional study.* A 3-D grid was built from the given 2-D data, and a 3-D FEM unconfined, saturated flow program was applied to the same problem with the 2-D and 3-D results then compared. This was done to help answer the question of when a 3-D solution is required for a given problem.
- b. *Cray Y-MP optimization.* Special vectorization techniques were investigated to see what improvements in running times could be achieved over the generic Unix version of the 3-D code. Computational improvements valid for any scientific computer were also made.
- c. *Scientific visualization.* Scientific visualization techniques were applied to the RMA data.

The 3-D computations were done on a Cray Y-MP using a modified version of a 3-D seepage/groundwater FEM program (Tracy 1991). Scientific visualization tools used were commercial programs such as Multi-Purpose Graphics System (MPGS) (Cray 1990) and customized software developed in the Scientific Visualization Center (SVC), WES. All scientific visualization was done on Silicon Graphics workstations.

Description of Problem

The problem consists of partially confined and partially unconfined groundwater flow in a region near RMA. The 2-D triangular mesh used for the problem is shown in Figure 1. The nodes with triangles have heads specified as a boundary condition, and the nodes identified with circles are observation wells where differing amounts of water are being extracted. The immediate purpose of the computation is a calibration where the unknown hydraulic conductivities are adjusted so that the initial heads remain the final heads after the problem is run to a steady-state solution. A slurry trench has been installed in the flow region to modify flow, and a zoom of the grid for this region is shown in Figure 2. The slurry trench is

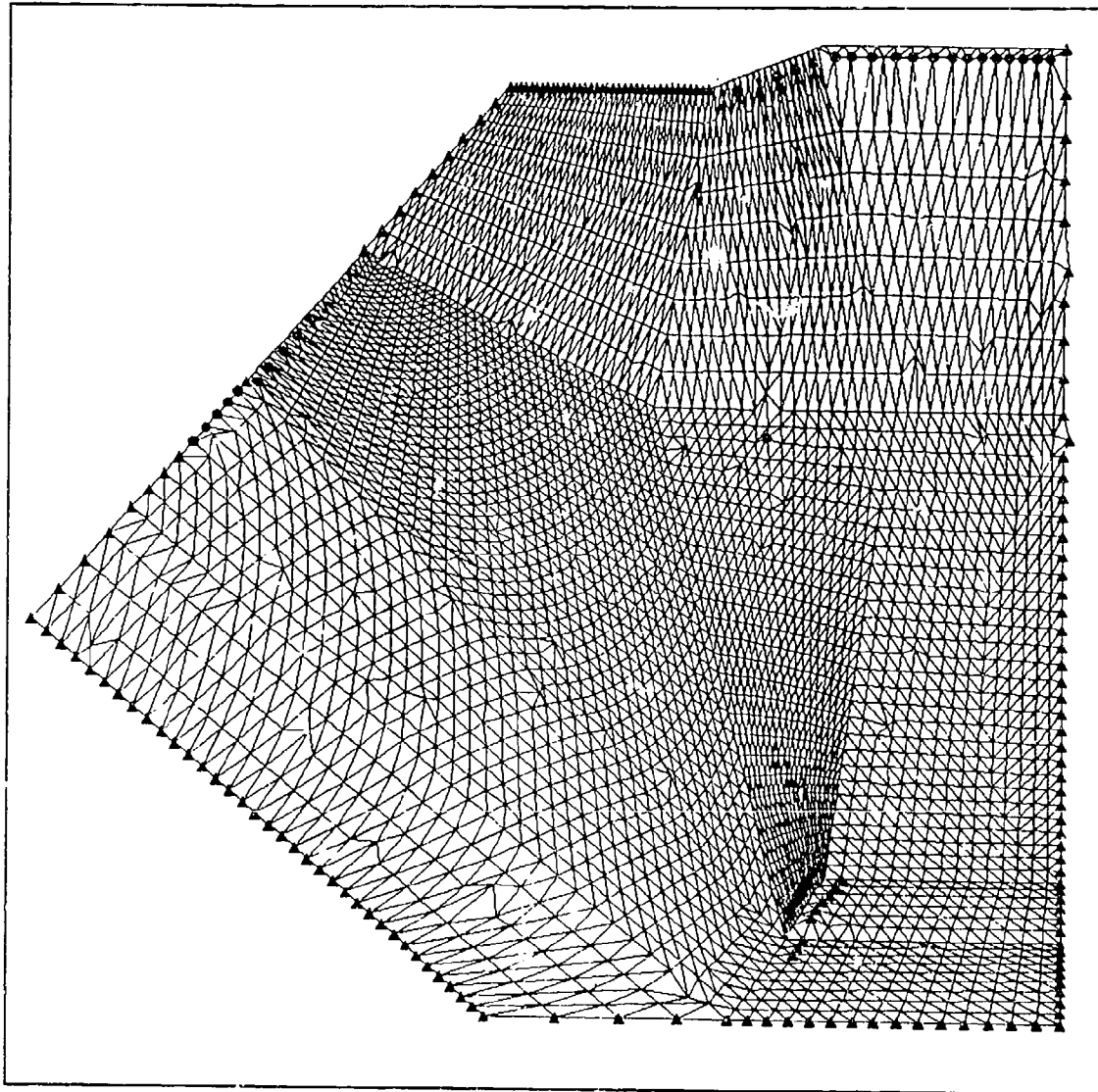


Figure 1. FEM grid with boundary conditions

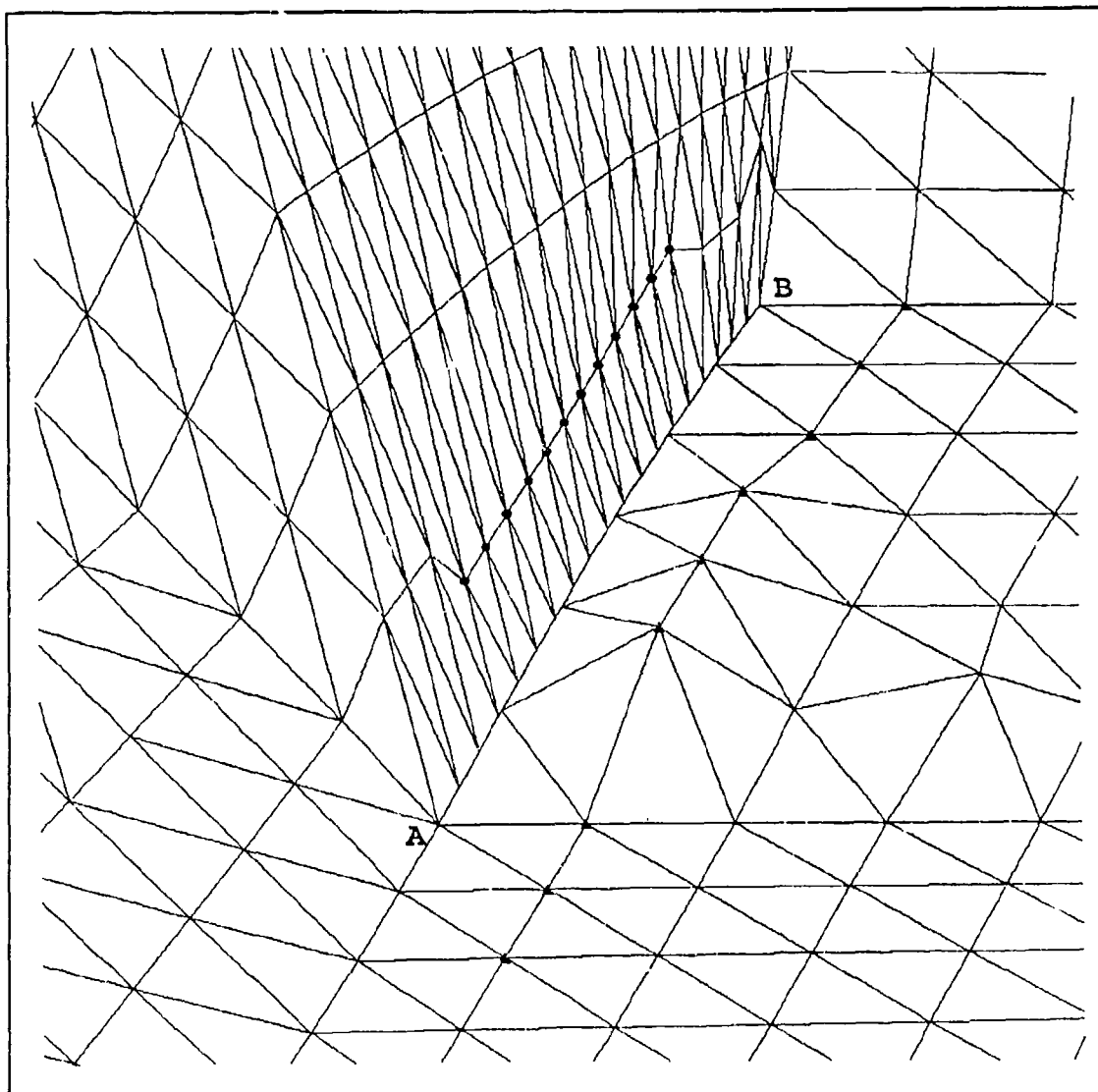


Figure 2. Zoomed area showing slurry trench

identified by all the nodes along line segment AB. An impervious wall such as a slurry trench is modeled by having different nodes on one side of the wall as compared to the other side. This particular slurry trench has many more nodes on the left side than on the right side.

There are two basic layers which are alluvium and bedrock. The hydraulic conductivities, however, vary greatly within these two broad categories of material. Figure 3 shows a color contour plot of the hydraulic conductivity of the alluvium, and Figure 4 shows a color contour plot of the hydraulic conductivity of the bedrock. Figure 5 shows a color contour plot of the initial total head values. The problem is now completely specified.

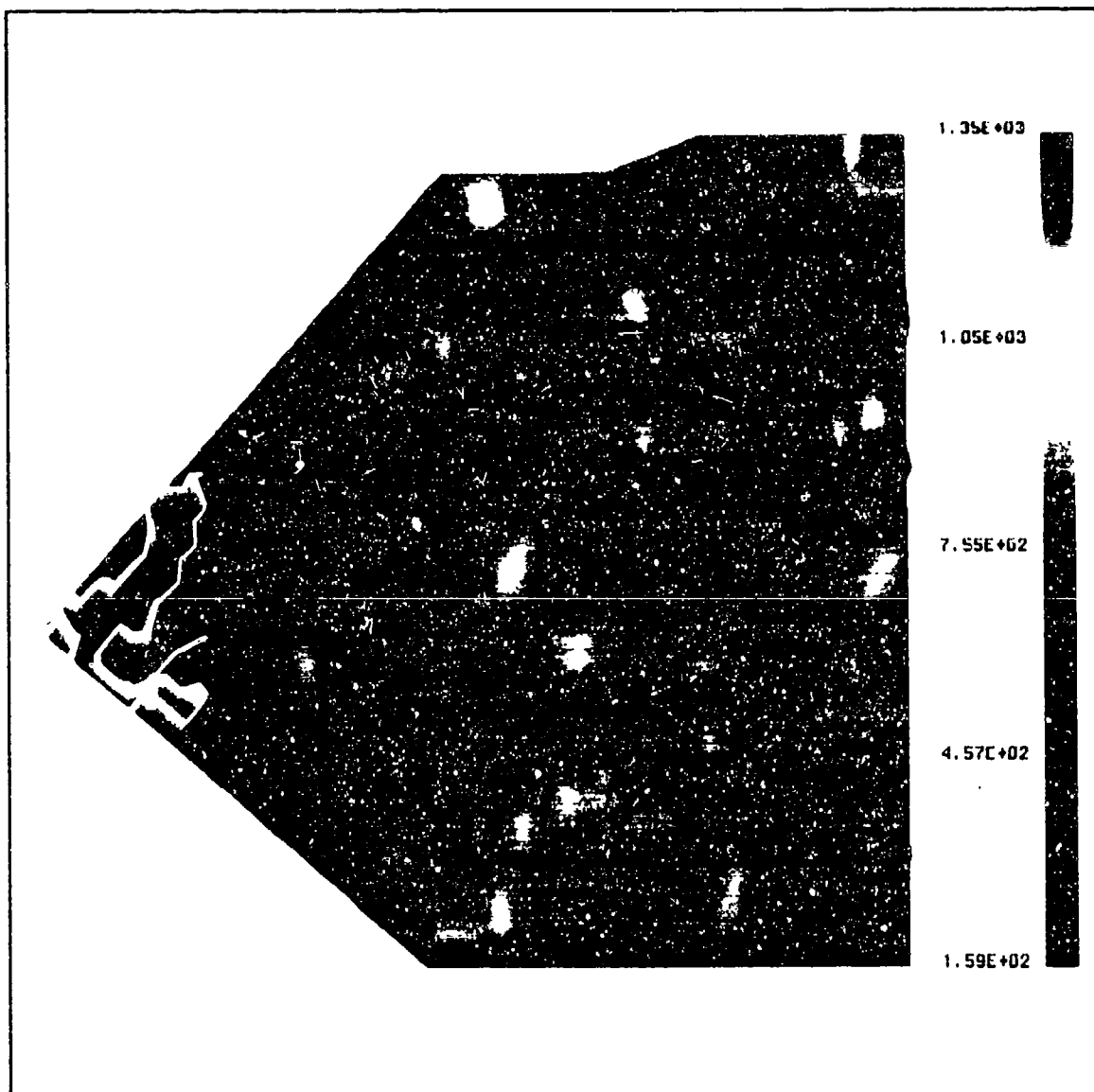


Figure 3. Hydraulic conductivity of the alluvium

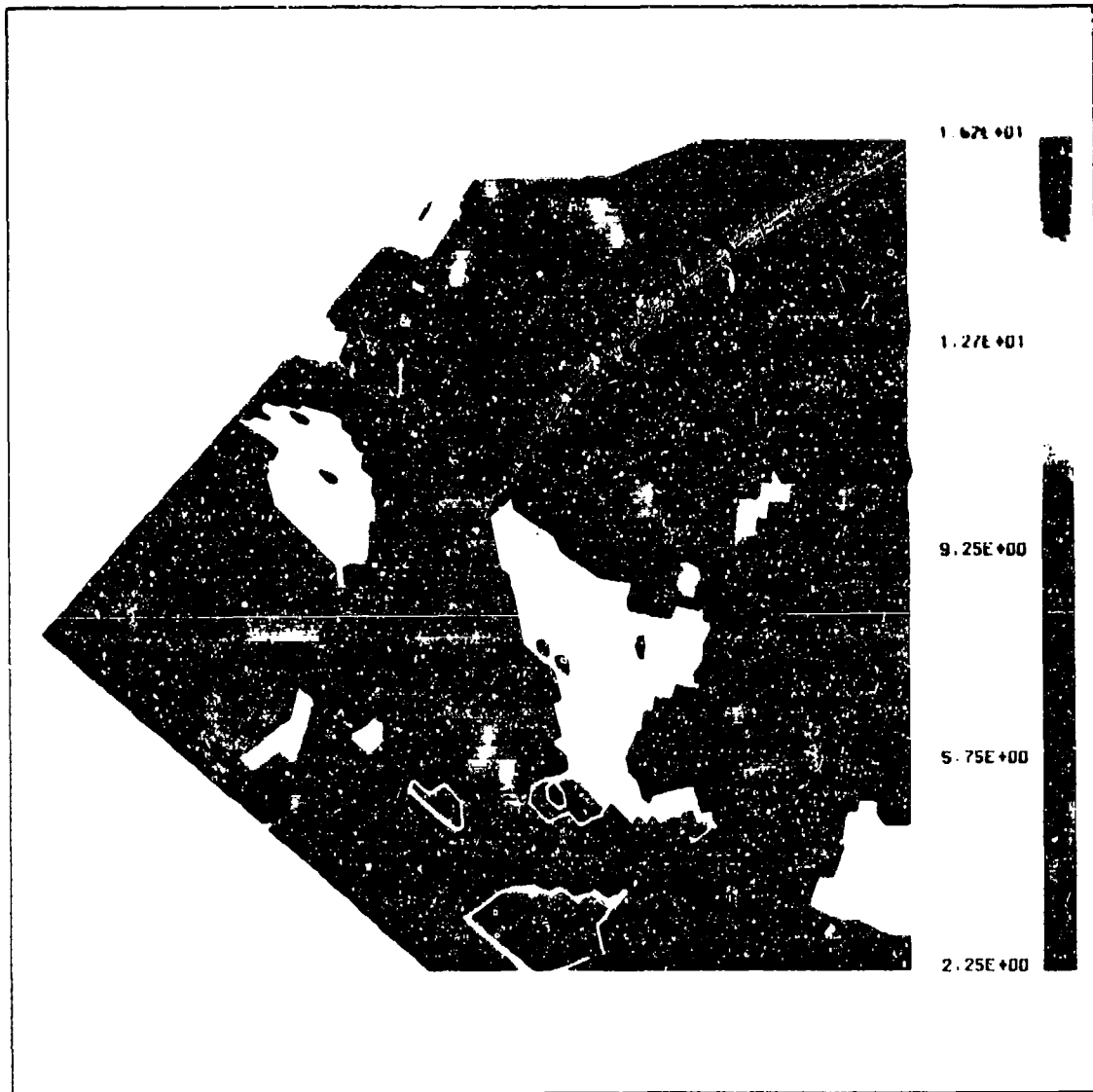


Figure 4. Hydraulic conductivity of the bedrock

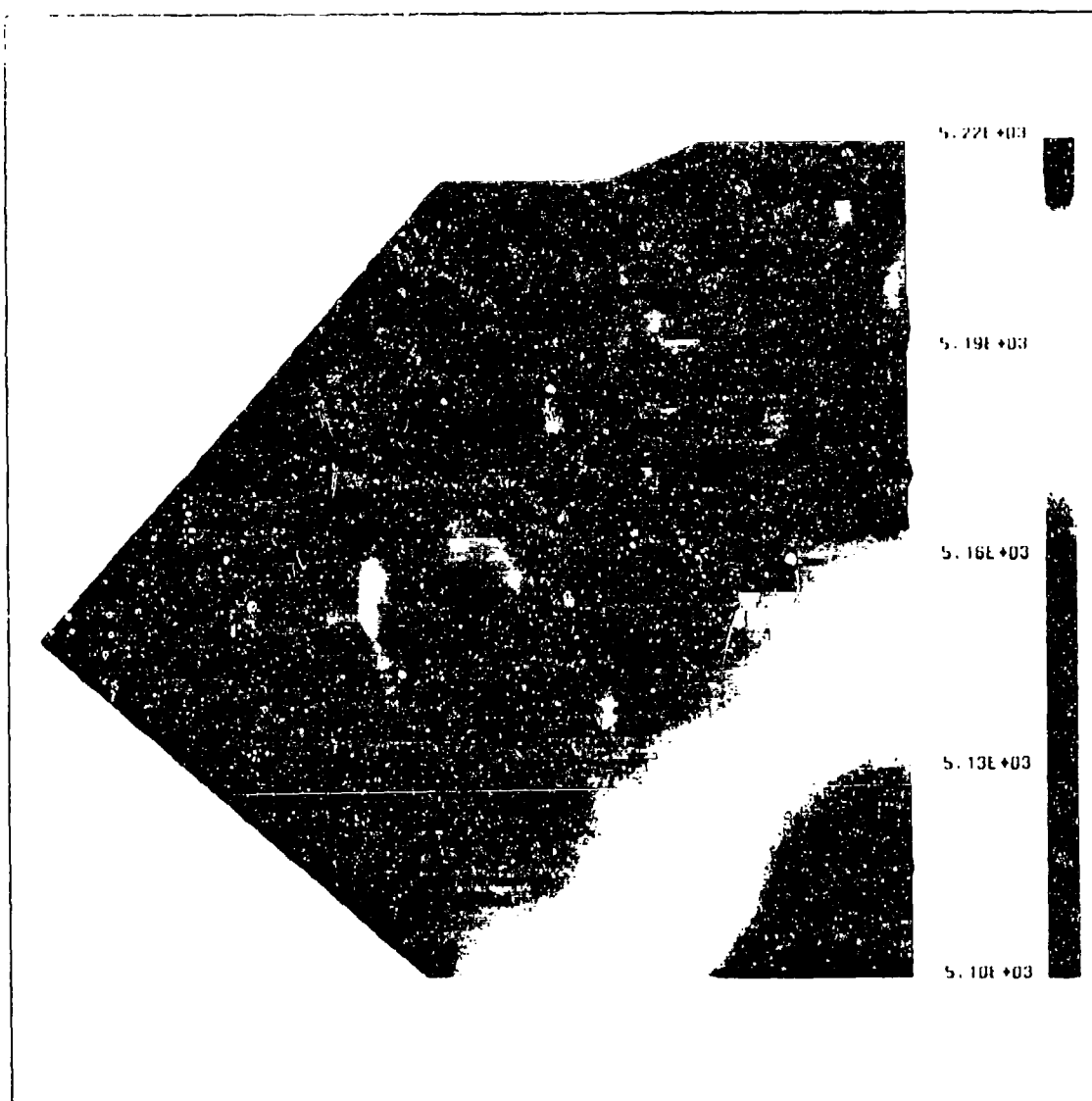


Figure 5. Initial head values

2-D Results

Figure 6 shows the results of one of the intermediate calibrations. The amount of drawdown is small in most places, but there are still some "hot spots" to fix. It is clear that the color contour plot is an excellent tool to quickly determine the areas that need more work. The final calibration will be presented in the GL report to RMA. The purposes of this chapter are well served by using these intermediate results, and the problem of using possibly proprietary information is avoided.

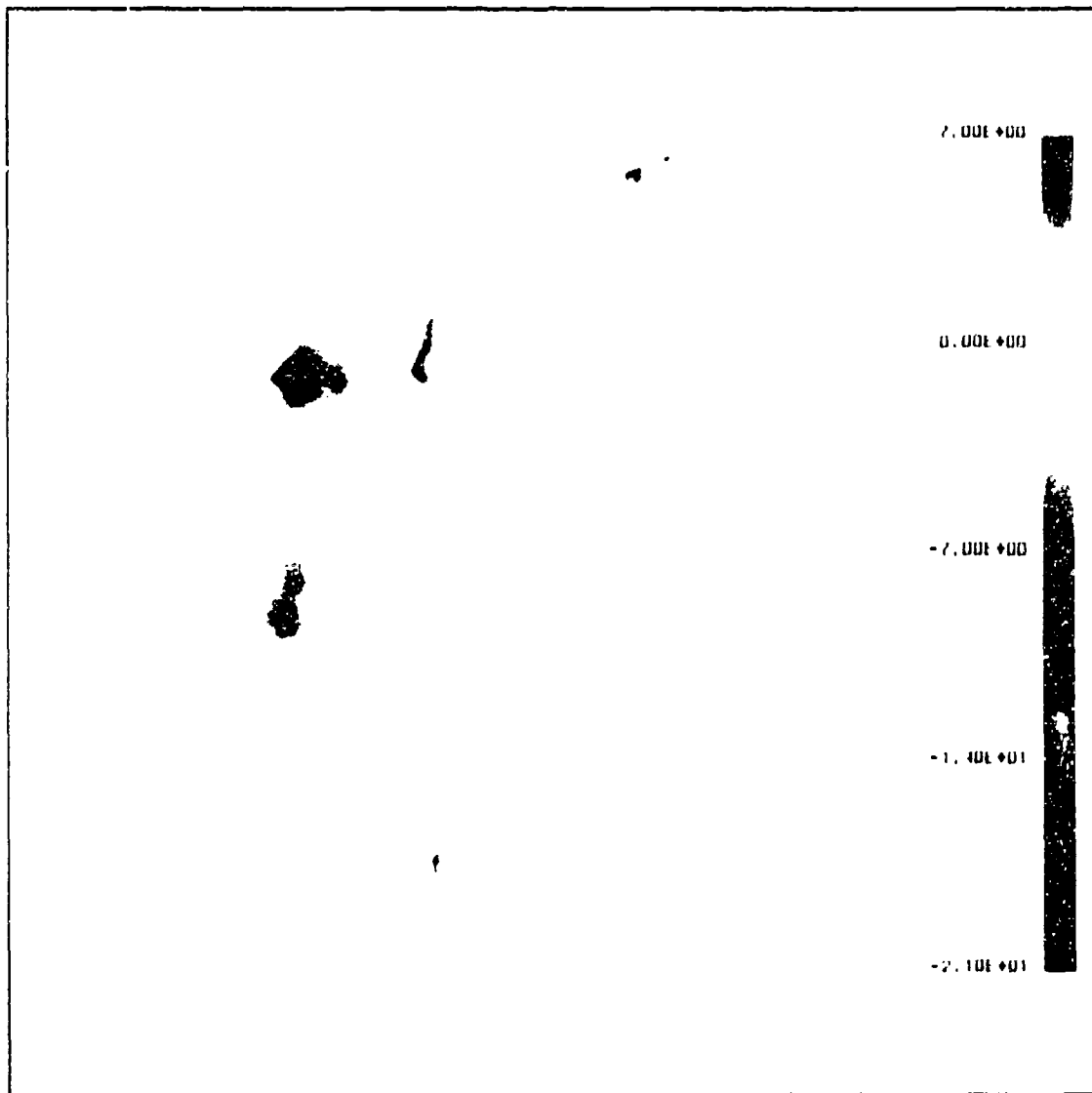


Figure 6. Intermediate calibration drawdown results

3-D Study

At this point a study was begun to determine how important a true 3-D solution is and how to visualize the 3-D results. Cray optimization was also investigated by personnel in the DoD High Performance Computing (HPC) Center group in ITL.

3-D grid

A 3-D grid was generated from the 2-D data by adding intermediate layers (see the hidden line view of the grid shown in Figure 7) by converting

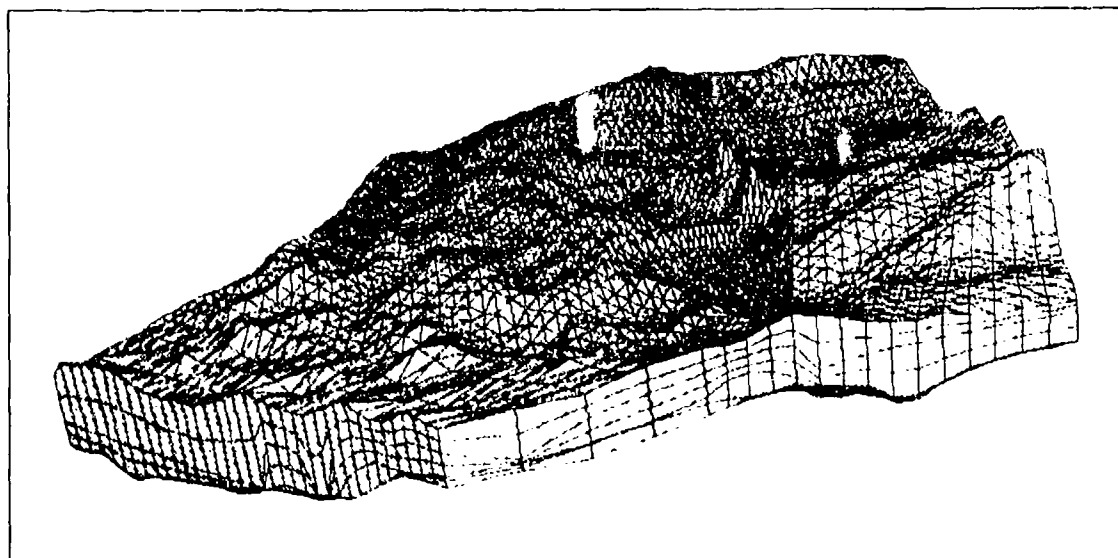


Figure 7 Hidden line view of the grid

2-D triangular elements into eight node brick elements with two sets of nodes repeated to form a prism as shown in Figure 8. A FORTRAN program was written to produce the 3-D grid and apply the appropriate boundary conditions. Each 2-D node was used to generate seven 3-D nodes, and each 2-D triangular element was used to generate six prisms. If a 2-D node has a specified head boundary condition in a confined flow region, then the seven generated 3-D nodes from that 2-D node are given the specified head. However, if a 2-D node has a specified head boundary condition in an unconfined flow condition in the alluvium, then the fourth and fifth generated 3-D nodes are adjusted so the elevation of the fifth node is the same as the specified head (see Figure 9), and only the first five 3-D generated nodes are given the specified head. In like manner, a 2-D node with head specified in the bedrock has the elevation of the second generated 3-D node modified to the specified head value, and only the first two generated 3-D nodes are given the specified head.

A 2-D node where an observation well exists and the flow Q is specified in a confined flow region has flow distributed over the generated 3-D nodes as if each of the vertical line segments in the alluvium collects the same amount of water. That is, generated 3-D nodes 3 and 7 have $Q/8$ specified, and generated 3-D nodes 4 through 6 have $Q/4$ specified. For a 2-D unconfined flow region node where the initial water level is in the alluvium:

- a. *Adjust elevations.* The elevations of generated 3-D nodes 4 and 5 are adjusted as before so the fifth node falls at the water elevation.
- b. *Distribute flow.* The Q this time is distributed so generated 3-D nodes 3 and 5 have $Q/4$, and generated 3-D node 4 has $Q/2$ applied.

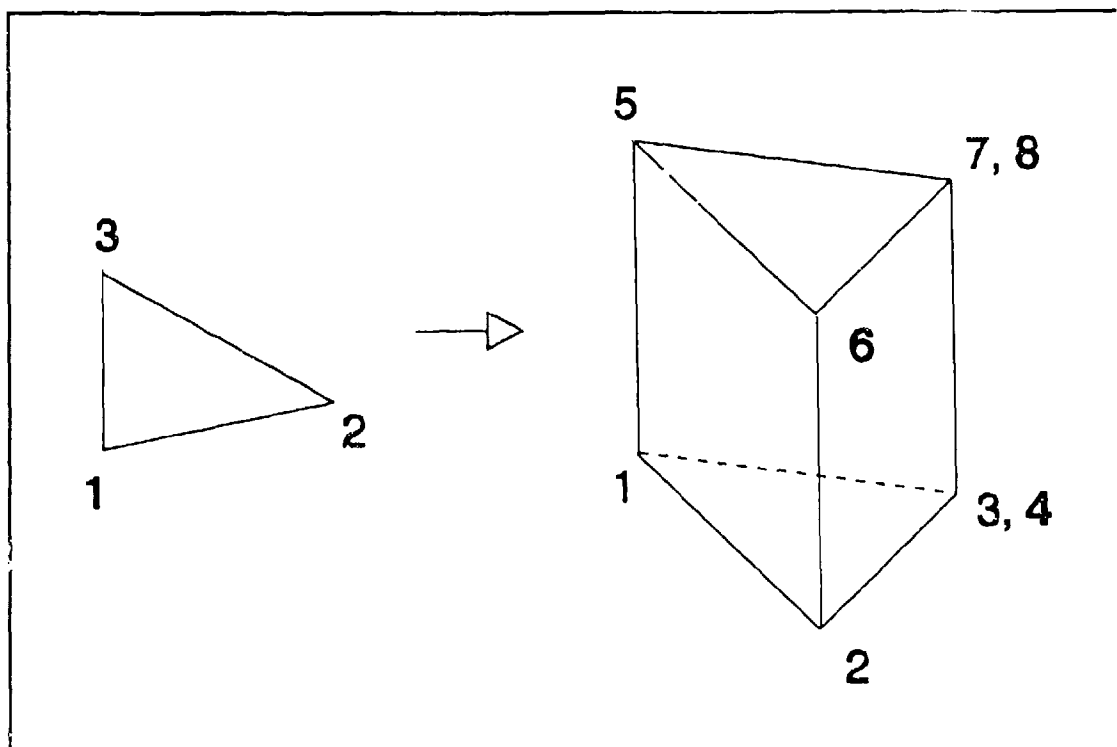


Figure 8. 2-D triangles converted to 3-D prisms

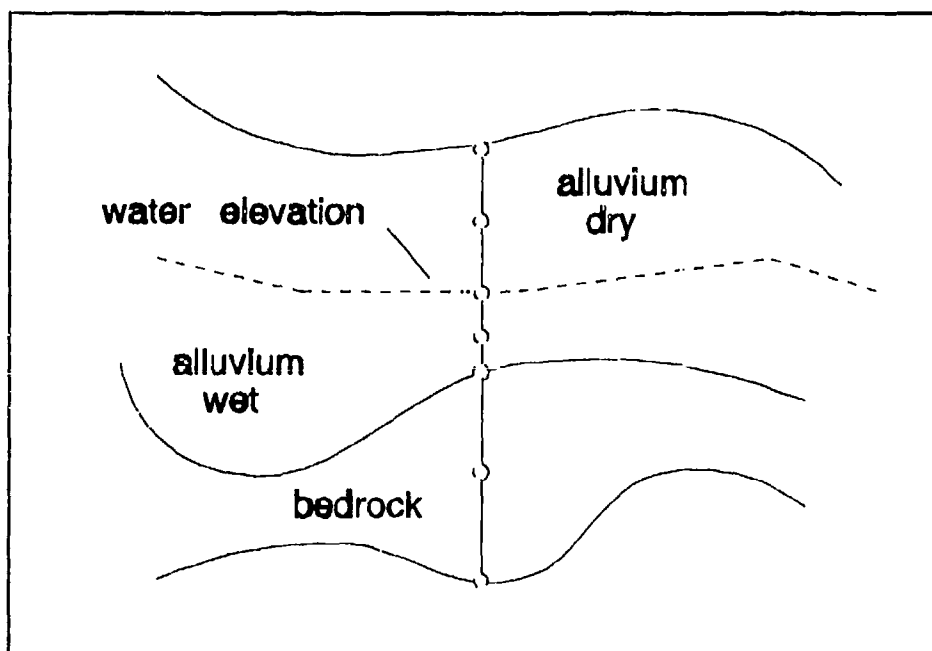


Figure 9. Specified head in alluvium

Since this is a calibration at a rather late stage, step *a* was not repeated at each iteration in the 3-D groundwater program to find the free surface. However, this should be incorporated into the program for doing studies beyond the calibration.

For an unconfined flow situation where the water table is in the bedrock, the elevation of generated 3-D node 2 is given the value of the water elevation, and the given *Q* is divided equally between generated 3-D nodes 1 and 2.

3-D groundwater model

The 3-D groundwater model used in this study is a modification of one written by this author for 3-D steady-state, unconfined saturated flow. The modifications required are as follows:

- a. *Hydraulic conductivity data.* Typically, in an FEM program, the material properties are specified separately, and each set is given a number. For instance, material type 1 can represent sand, and material type 2 can represent clay. Thus, each element has a material type number specified, and those values specified remain constant inside the given element. The data for RMA is different. There were provided one hydraulic conductivity for bedrock and one hydraulic conductivity for alluvium for each 2-D node. Therefore, no data were provided for element properties, but the node data were extended to include the two hydraulic conductivities. However, each element still had to be identified as being either bedrock or alluvium.
- b. *Stiffness matrix computation.* Since hydraulic conductivity is not constant inside each element, the stiffness matrix computation had to be modified. The material type number for each element now represents either 1 for bedrock or 2 for alluvium. The finite element type used in the 3-D model requires numerical integration to form the stiffness matrix. So at integration point *j*, the hydraulic conductivity k^j is computed using the eight-node isoparametric element formulation

$$k^j = \sum_{i=1}^8 N_i k_i \quad (1)$$

The interpolation functions are

$$N_{ij} = \frac{1}{8} (1 + \xi_i \xi_j) (1 + \eta_i \eta_j) (1 + \zeta_i \zeta_j) \quad (2)$$

where

$$\begin{pmatrix} -1 \leq \xi \leq 1 \\ -1 \leq \eta \leq 1 \\ -1 \leq \zeta \leq 1 \end{pmatrix}$$

$(\xi_i, \eta_i, \zeta_i) = (\xi, \eta, \zeta)$ coordinates at node i

$(\xi_j, \eta_j, \zeta_j) = (\xi, \eta, \zeta)$ coordinates at interpolation point j

k_i = hydraulic conductivity at node i

- c. *MPGS files.* MPGS files were written for the original grid, the modified grid that conforms to the free surface, a scalar file containing total head, and a vector file containing Darcian velocities.

Visualization of 3-D results

After a valid 3-D grid was produced and a correct 3-D groundwater model was completed, the 3-D results were obtained. It is, of course, now very important to visualize the resulting voluminous set of output data. It is extremely difficult to visualize 3-D groundwater flow for the following three reasons:

- a. *Relatively flat grid.* The 3-D grid in the z direction is extremely flat compared to the plan view.
- b. *No specific object.* In computational fluid dynamics (CFD) there are airplanes, helicopters, etc., that form an excellent background for visualization. However, in groundwater flow no such tangible objects exist.
- c. *Heterogeneity.* In CFD applications there is only a single homogeneous medium such as air. Flow in porous media deals with significantly different properties which, at times, varies several orders of magnitude.

Nevertheless, the following give a good representation of the flow pattern:

- a. *Color contours.* Color contours on visible faces used to show variation of scalar quantities.
- b. *Isolevels.* The 3-D equivalent of a contour plot where each isolevel in space is a surface representing a scalar quantity with the same value.

- c. *Particle traces.* Lines in space that show the paths of particles after being released in the porous medium.
- d. *Translucency.* The ability to see through an object or data to see what is behind it.
- e. *Animation.* Viewing many scenes (30 frames per second) in succession showing movement of rotation, translation, flow, etc.

As examples, Figure 10 shows the hidden line plot of the grid with total head in color contours, and Figure 11 shows the 3-D grid as translucent with three isolevels. The fact that the isolevels are essentially vertical shows that there is little variation of the results in the z direction.

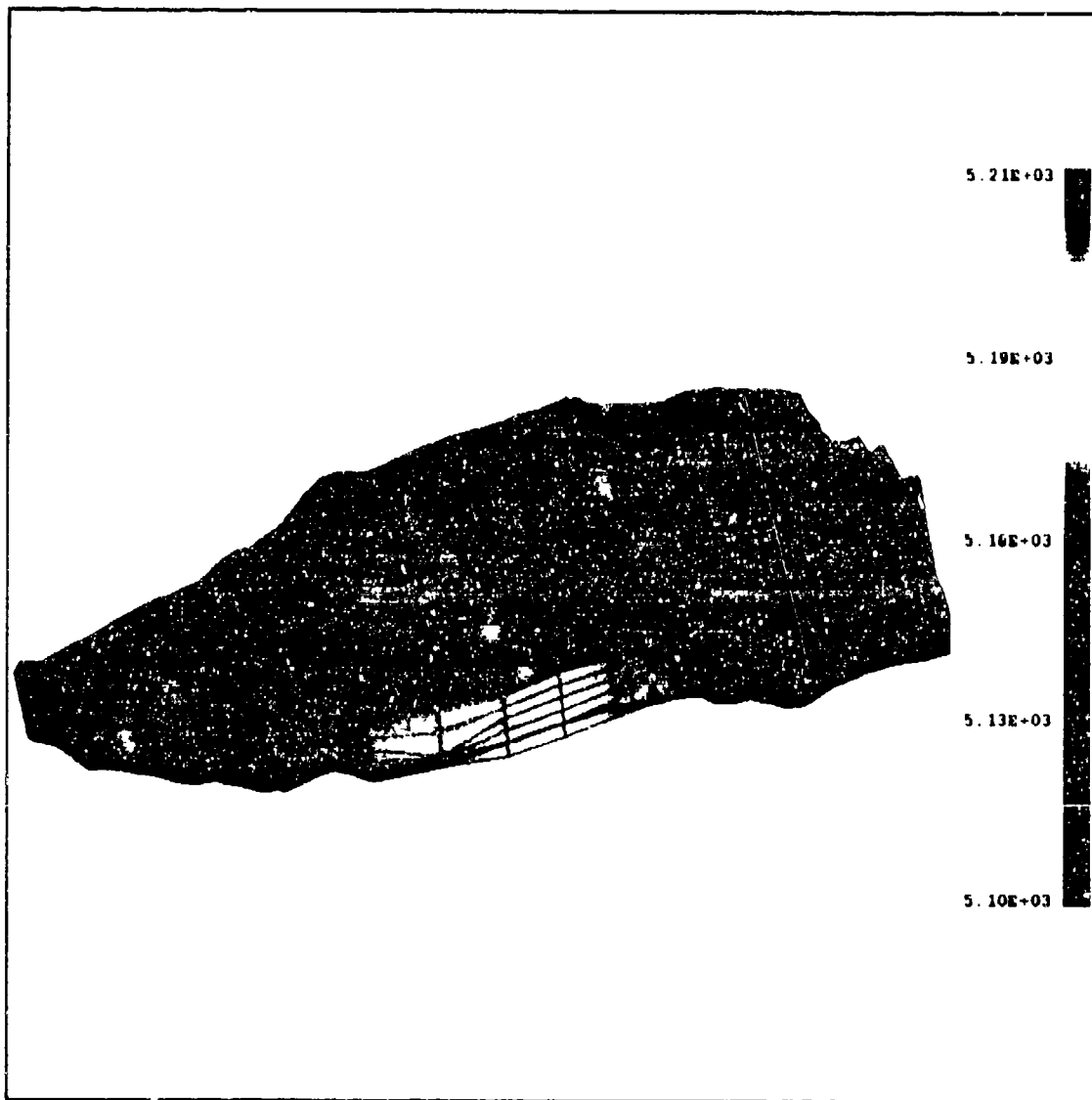


Figure 10. Total head contours with the hidden line plot



Figure 11. Translucent grid with isolevels

Cray Y-MP improvements

Performance issues were addressed by Mr. Alex Carrillo, HPC Center, WES. For evaluation purposes, in addition to the RMA groundwater model, a smaller aquifer groundwater model and two different grid sizes of the Cerrillos Dam in Puerto Rico seepage model were used (the Cerrillos Dam study was performed by Mr. John Palmerton, GL, WES). Table 1 describes various aspects of the models. First, the number of nodes and elements for each model is given. Next, the number of nonlinear iterations required to obtain the steady-state solution is given. Each iteration can be summarized as formulating and solving the following set of equations:

$$[K]^i \{\Delta\phi\}^i = -\{\Delta Q\}^i \quad (3)$$

$$\{\phi\}^{i+1} = \{\phi\}^i + \{\Delta\phi\}^i$$

Table 1
Model Information

| Model | RMA | Aquifer | Cerrillos (Small) | Cerrillos (Big) |
|----------------------------------|--------|---------|-------------------|-----------------|
| Nodes | 23,513 | 11,578 | 10,915 | 87,572 |
| Elements | 38,796 | 9,855 | 8,469 | 77,124 |
| Nonlinear Iterations | 48 | 5 | 8 | 9 |
| Original Global Bandwidth | 883 | 1,594 | 502 | 1,974 |
| Original Average Local Bandwidth | 364 | 1,075 | 467 | 1,855 |
| New Global Bandwidth | 482 | 675 | 303 | 1,481 |
| New Average Local Bandwidth | 356 | 436 | 283 | 1,092 |
| Original CPU | 12,548 | 3,747 | 517 | 33,148 |
| Original I/O | 5,149 | 910 | 273 | 8,040 |
| New Direct Solver CPU | 188 | 33 | 47 | 3,906 |
| New Direct Solver I/O | 30 | 1 | 1 | 1,235 |
| New Iterative Solver CPU | 594 | 29 | 21 | 278 |
| New Iterative Solver I/O | 0 | 0 | 0 | 0 |

where

$[K]^i$ = stiffness matrix at the i 'th iteration

$\{\Delta\phi\}^i$ = change in total head or potential vector at the i 'th iteration

$\{\Delta Q\}^i$ = residual flow vector at the i 'th iteration

Because the solution is steady state, a significant savings can be achieved by updating $[K]^i$ only with respect to changing boundary conditions, and this is done. $\{\Delta Q\}^i$ must, however, be computed using the current values of the element stiffness matrices.

The initial profiling of the code revealed that the primary area affecting performance was the solution process (the solution of the set of simultaneous linear equations in Equation 3). Not only was this part a computational bottleneck, but the I/O required for the out-of-core solver also severely inhibited performance. The I/O for storing stiffness and other matrices was also a significant factor. Thus, formulating and solving Equation 3 with the accompanying I/O, along with some standard improvements, were the primary focus of the evaluation and modifications. In fact, many of the improvements made to the program apply equally well to a generic engineering workstation as well as a supercomputer.

Solution process. Changes to the solution algorithm branched into two directions. First, a more efficient direct solver, a Cholesky factorization, was used to replace the Gaussian elimination routine being used in the original program. Secondly, a preconditioned conjugate gradient-like method was added to provide an iterative solver capability. Various problem characteristics affected the performance of each method. The Cholesky factorization routine was developed using a LAPACK library subroutine (Anderson, et al. 1990) as a template. Using this new algorithm, the grid was first divided into 64-node blocks. Then, an out-of-core capability was built around the routine, and minor modifications were made to take advantage of the smaller local bandwidth of each block. Also, for an unchanging stiffness matrix between nonlinear iterations, reuse of the factorization from the previous iteration greatly reduced the computations required for some problems. Coupled with a more sophisticated bandwidth minimization routine (Gibbs, Poole, and Stockmeyer 1976), significant time reductions were obtained for the direct solution process. (Table 1 shows both the global and average local bandwidth using both the original and the new bandwidth minimization routines.)

The introduction of the preconditioned conjugate gradient-like method added an iterative solver capability. The reduced memory requirements of this method eliminated the need for an out-of-core solution. Not as stable as the direct solvers, the iterative solvers can have problems converging

for poorly conditioned problems. However, for large, well-conditioned problems, they can perform significantly better than the direct solvers.

I/O. Several changes were made to improve the I/O and memory management of the program. First, the stiffness matrix was switched from a banded storage format to a sparse matrix format. This allowed assembly and boundary condition modifications to be completed in-core and eliminated many of the inefficiencies associated with the out-of-core solver. This also allowed a simpler transition between the iterative and direct solvers. The reduced bandwidths also decreased the I/O requirements for the out-of-core solver, making the use of faster disks more feasible. Finally, the iterative solver eliminated the need of any out-of-core I/O time altogether.

General improvements. Enhanced vectorization and other improvements in coding were also accomplished. Through effective use of arrays, redundant work was eliminated, and several functions were transformed into level 3 BLAS routines (Dongarra, et al. 1990).

Results. Table 1 shows the CPU times and I/O wait times (in seconds) for the original program, the new program using the direct (Cholesky) solver, and the iterative (preconditioned conjugate-like) solver. Specific characteristics of each problem produced the performance differences between the direct and iterative solvers. In general, however, the iterative method is preferred for large, well-conditioned problems. The RMA model tended to produce a poorly conditioned stiffness matrix, resulting in the iterative method having a difficult time converging. The stiffness matrix also remained unchanged for all the 48 nonlinear iterations, so substantial benefit was obtained from the reuse of the initial factorization. Thus, the direct solver provided the best performance. The aquifer model was well-conditioned, greatly improving the performance of the iterative method. It, too, benefitted from the reuse of the previous factorizations when using the direct solver, because only the first two nonlinear iterations required a factorization. The net result was a comparable time between the direct and iterative solvers. The Cerrillos dam models were also well-conditioned. However, in neither case did the stiffness matrix remain unchanged, explaining the superior performance of the iterative solver.

2-D Versus 3-D Comparison

A very important aspect of this research is to determine whether a 3-D study is needed in the saturated flow portion of GL's RMA modeling effort. Figure 12 is a color contour plot showing the difference in total head values between the 2-D and 3-D results. A 3-D result for a given 2-D node was obtained by averaging the values of head for the seven 3-D nodes corresponding to the 2-D node. The scale is set this way so that the plot can be directly compared to another plot described later in this report.

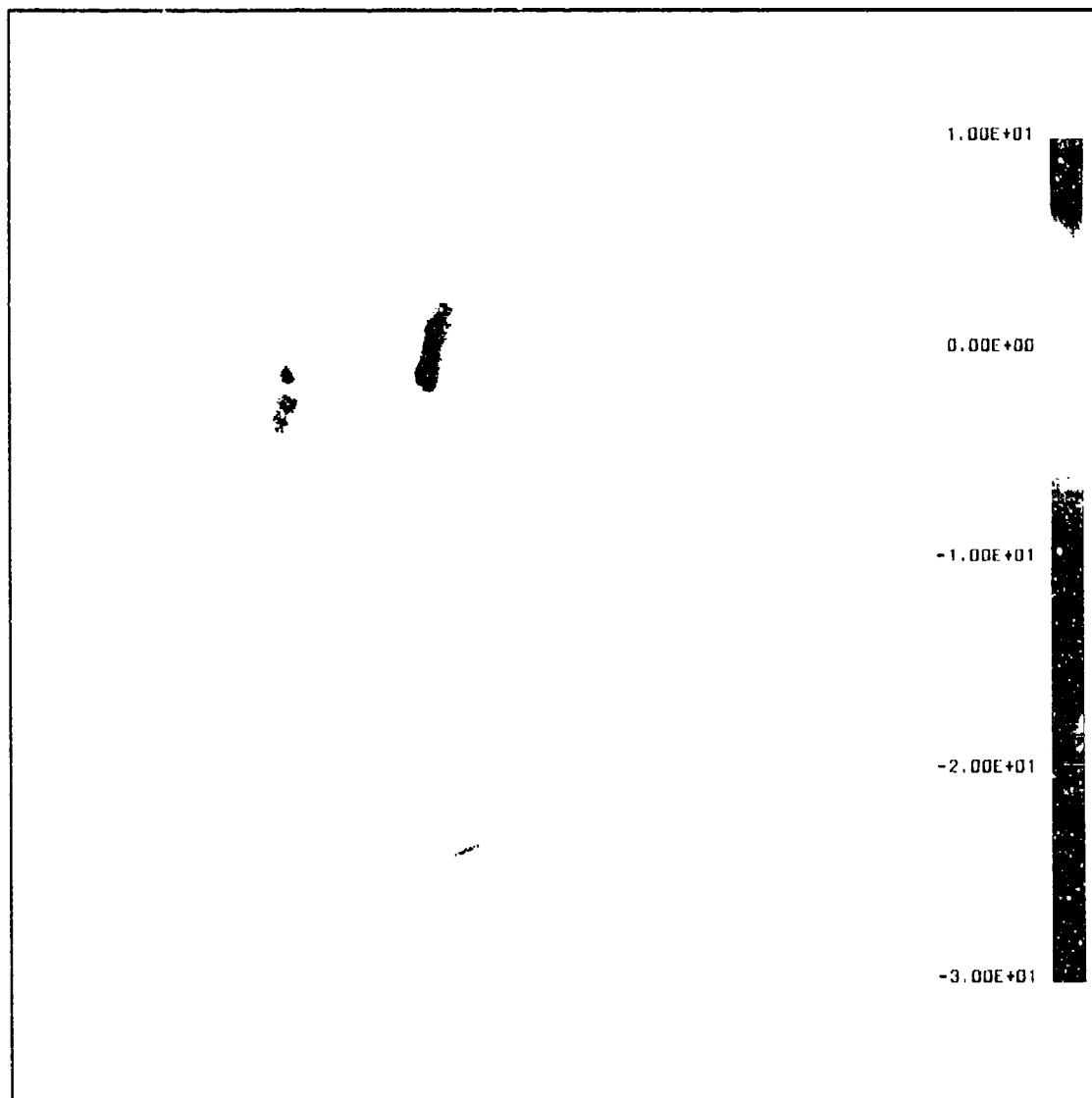


Figure 12. 2-D versus 3-D comparison

Yellow is selected as the color of no difference. While this is the dominant color, the maximum difference of about 10 ft (3.048 m) exists in some areas. Some variation is expected, so this amount seems reasonable. It is important to realize, also, that the boundary conditions are essentially 2-D boundary conditions. Head is specified a constant for the entire vertical area where head is known. True 3-D boundary conditions would have, for instance, a river specified more accurately.

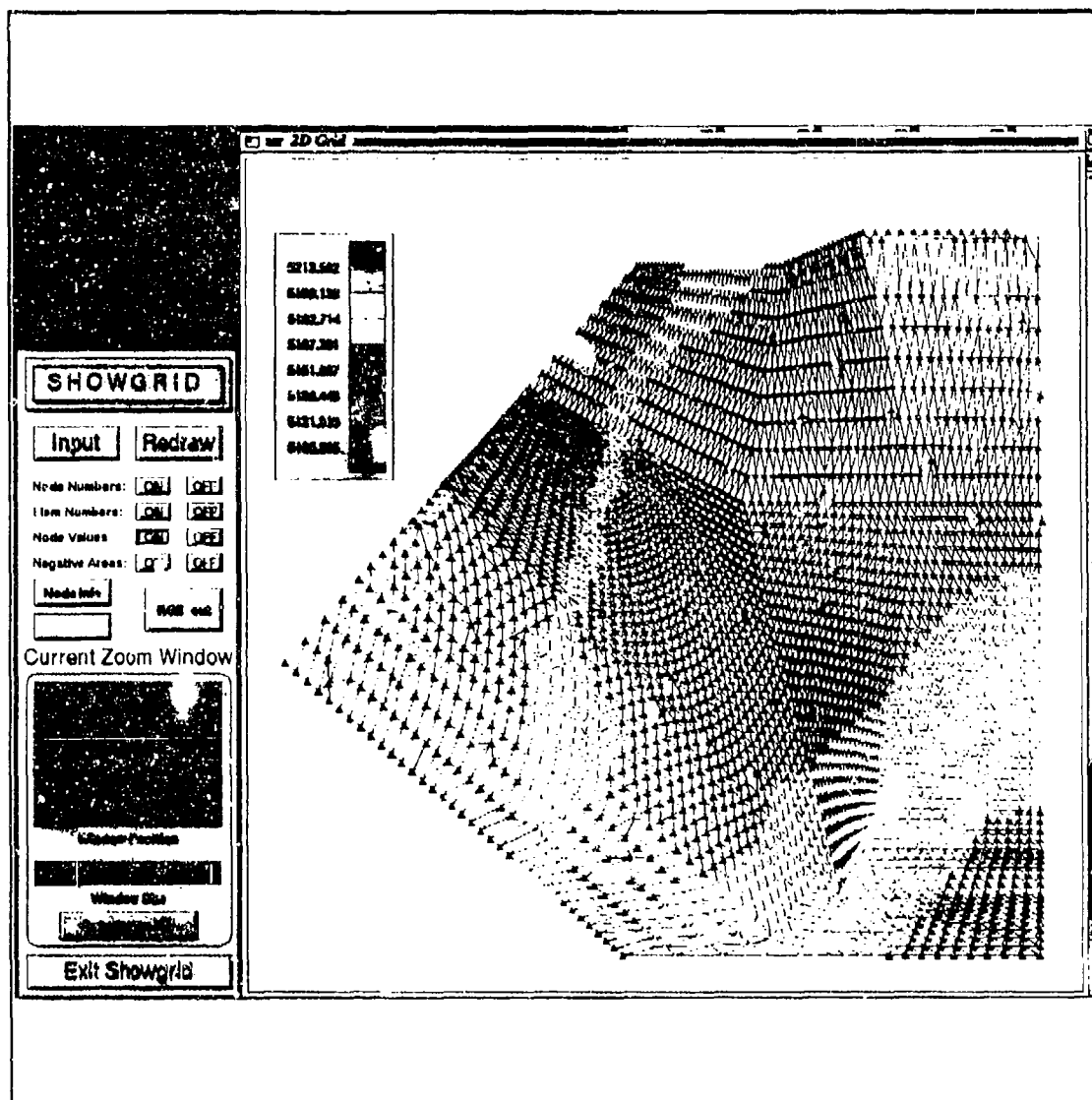
Grid Display

One of the most important graphics tools to use in doing an FEM model study is a program to display and edit the FE grid and other input data. There are many software and hardware options for this, and the topic may even seem a bit trite to some. However, because the author believes so strongly in the use of scientific visualization tools not only for understanding the results but also for ensuring the input data are correct, this section is included. Since results from the commercial package MPGS have already been shown, what is featured here is a quickly written (a few days) program called SHOWGRID. This program was written by Mr. Scott D. Weberg, SVC, for the Silicon Graphics workstation using their Graphics Language software. SHOWGRID can be used to view the 2-D grid, its boundary conditions, any scalar value, and any negative area elements. Figure 13 shows a plot of the menus developed with initial head being plotted for the node values. This can be compared with the color contour plot from MPGS given in Figure 5. Figures 1 and 2 are also SHOWGRID plots.

The primary problem that occurs with the grid is negative or badly skewed elements. Figure 14 shows a typical "bad spot" where the location of an observation well could have been accidentally moved so much that a negative area element was created (highlighted element 1056). With programs like SHOWGRID, these errors can be easily spotted and corrected. What is more difficult, however, is the detection of badly skewed elements. Figure 15 shows a zoomed area of the grid where an extremely skewed element has been created, and Figure 16 shows how this is fixed. Numerically, skewed elements such as these can cause severe problems, and they should be avoided. However, the triangular elements turned out to be much less susceptible to this than the brick elements with coincident nodes. This is illustrated by the 2-D versus 3-D comparison (Figure 17) for a grid containing several skewed elements like that of Figure 15. As before, one would expect some differences in the two solutions, but the rather large regions where significant differences occur were always caused by skewed elements in the 3-D grid (the 2-D solutions were essentially the same for the two cases). In fact, the large area where the difference is as much as 30 ft (9.144 m) (dark blue region) was completely turned to yellow by fixing the one skewed element shown in Figure 15. Figure 12, corresponding to the good grid, can be directly compared to the plot in Figure 17 to see the dramatic effect of fixing all such elements.

Summary and Conclusion

The 3-D study showed that for a large plan view flow problem where essentially 2-D type boundary conditions (a constant head is applied the full depth of the aquifer and fully penetrating wells are used) are employed, a 3-D solution is not usually necessary for the flow computations.



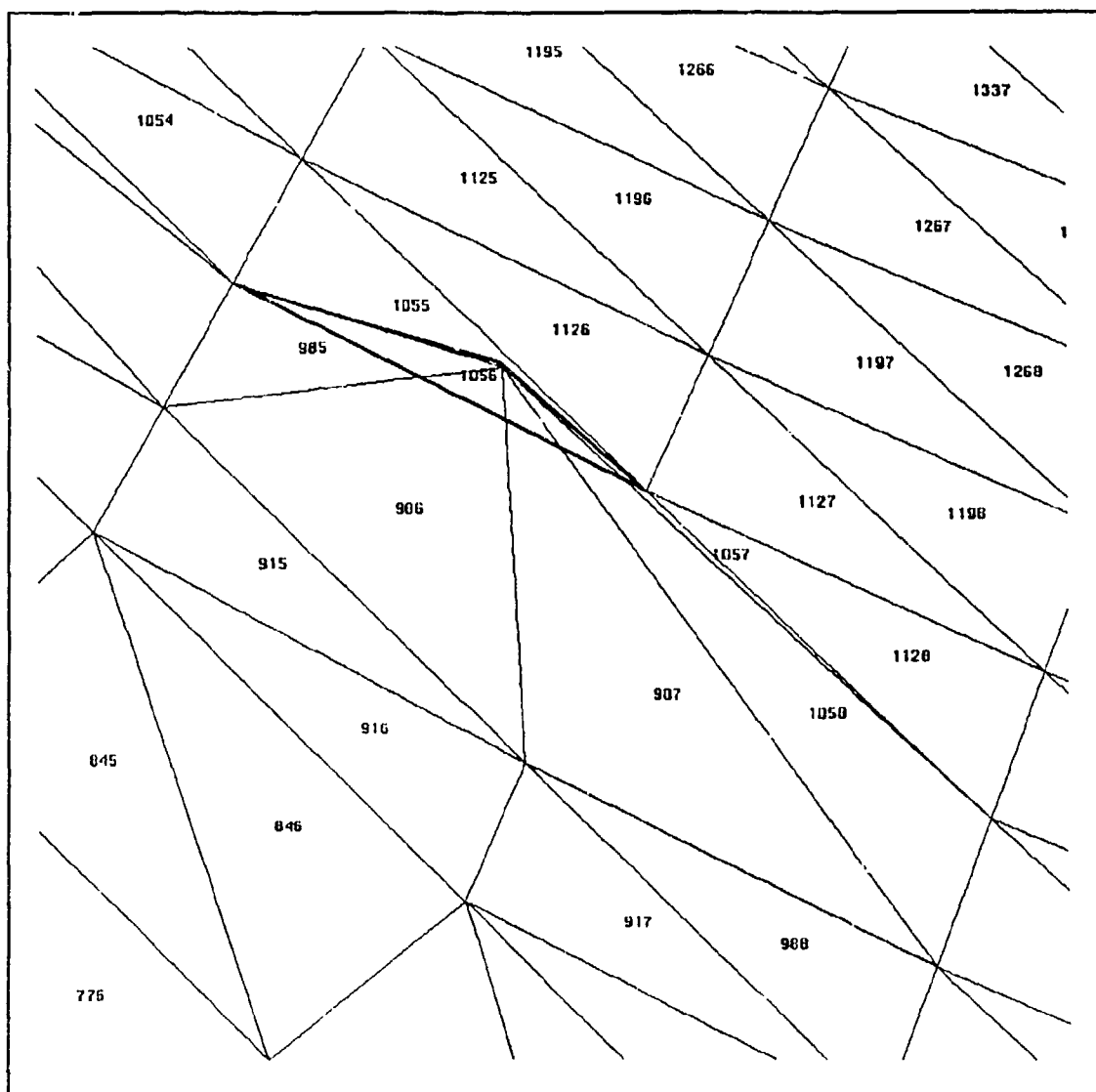


Figure 14. Negative area region

Two-dimensional triangular elements are more stable than nine-node brick elements with coincident nodes with respect to skewness. A 3-D prism or tetrahedron element should be considered, or a careful examination of the 2-D grid is required.

This exercise has also shown that visualization tools are essential when doing a numerical study to both ensure the correctness of the input data and to properly interpret the results. Further, without the use of a large scientific computer such as the Cray Y-MP, a full study of a large 3-D problem is almost impossible. This is especially true of time-dependent nonlinear multiphase flow and contaminant transport computations.

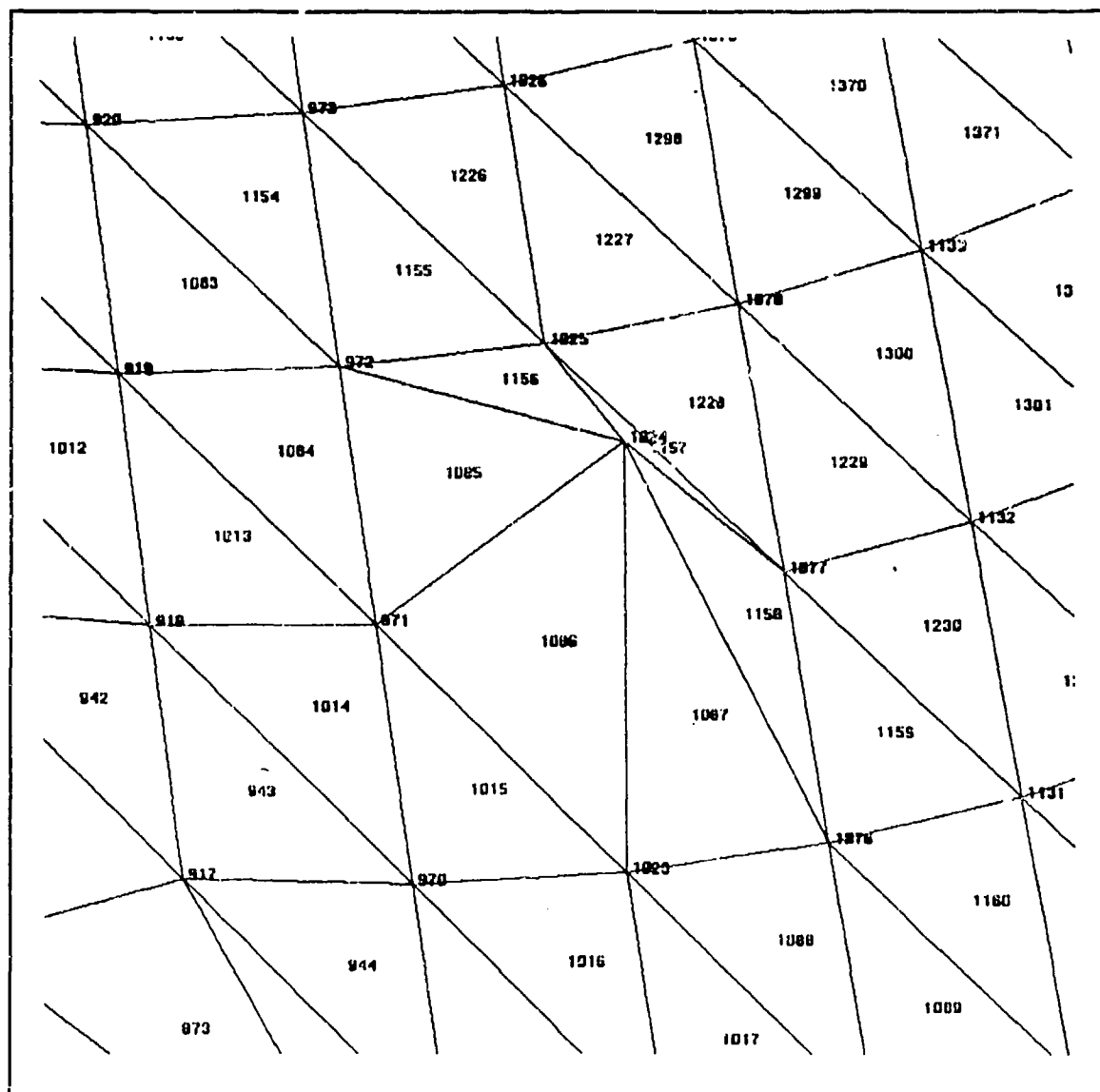


Figure 15. Skewed element

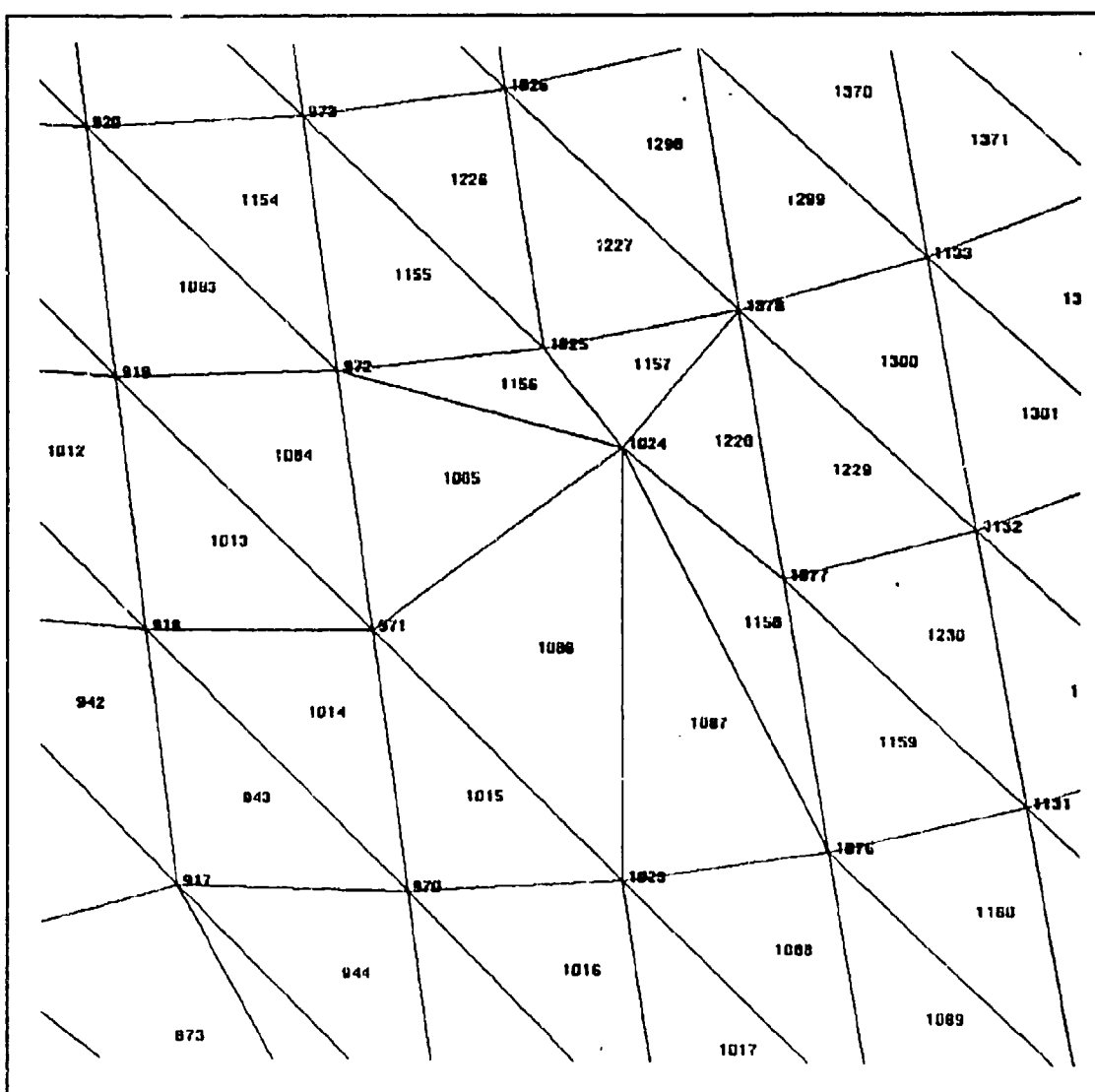


Figure 16. Fixed elements

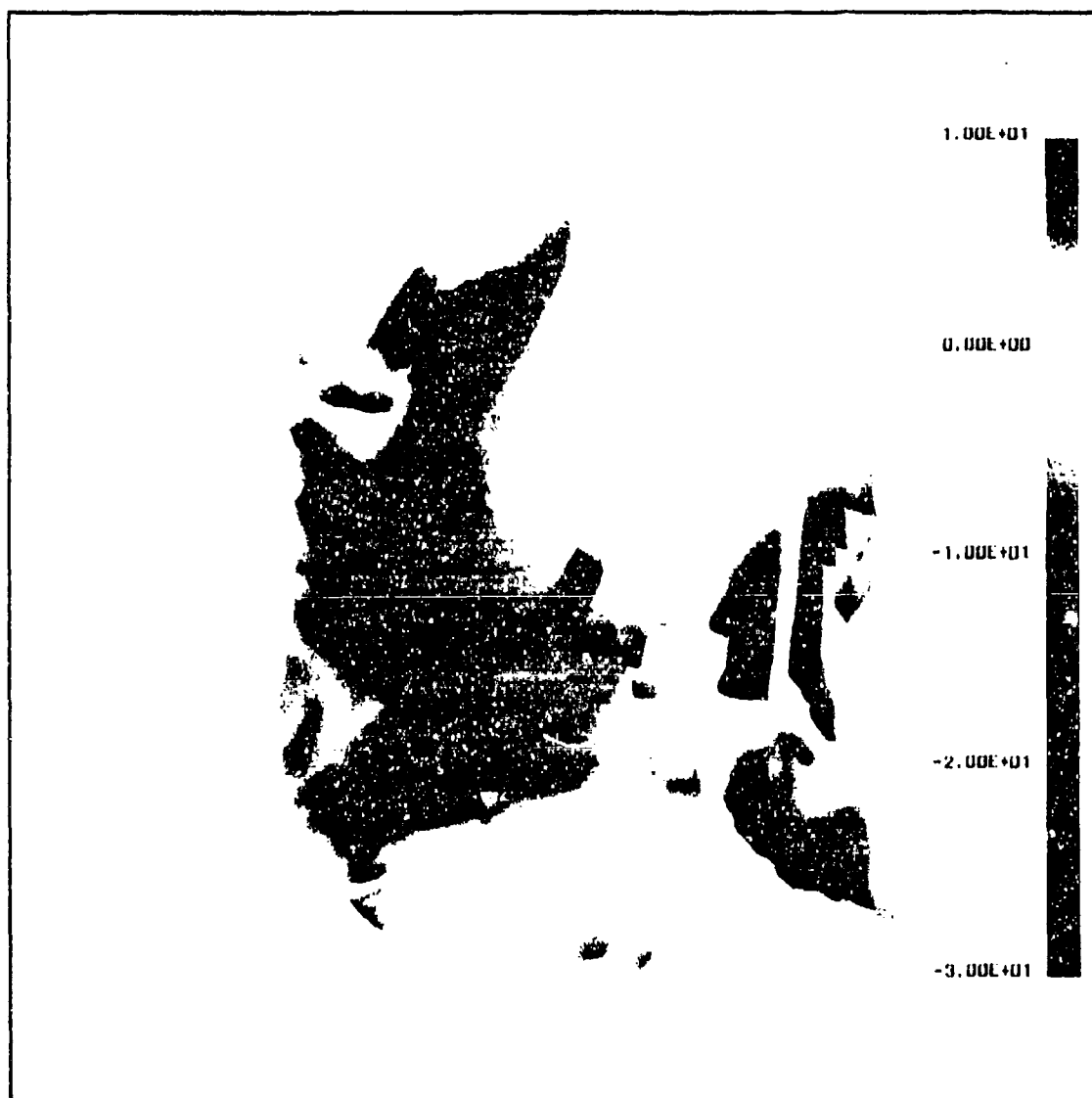


Figure 17. 2-D versus 3-D comparison with skewed elements

3 Unsaturated Flow

Introduction

Chapter 2 gave some extensive work using the FEM for saturated flow. This chapter will investigate unsaturated flow using another computational technique typically used by the aerospace engineers, which is the finite volume method (FVM). The FVM is very similar (and sometimes identical) to the finite difference method. The following will be presented:

- a. *Governing equations.* The equations used in this work to model the unsaturated flow cast in strong conservative form for a curvilinear coordinate system.
- b. *Computational procedure.* The finite volume equations used to idealize the governing equations and the numerical scheme used to solve them.
- c. *Comparison of results.* Results obtained from this FVM technique are compared with FEM results for various problems, including laboratory tests and analytical solutions.

Governing Equations

The governing partial differential equation used for unsaturated flow for both the (x, y, z) and the (ξ, η, ζ) curvilinear coordinate systems will now be given.

(x, y, z) equations

The equation at a given (x, y, z) point in space and time t in matrix form is

$$\nabla^T \{k_r [k_s] (\nabla h + \nabla z)\} + q = F \frac{\partial h}{\partial t} \quad (4)$$

where

h = pressure head

$[k_s]$ = saturated hydraulic conductivity matrix

k_r = relative hydraulic conductivity

q = source or sink

F = water capacity given by

$$F = \frac{d\theta}{dh} \quad (5)$$

where θ = is the moisture content

In an unsaturated zone of flow, F and k_r are functions of h , making Equation 4 highly nonlinear. Equation 4 is also at times put in terms of the total head or potential ϕ

$$\phi = h + z - \phi_d \quad (6)$$

where ϕ_d = datum

Equation 4, using Equation 6, now becomes

$$\nabla^T \{k_r [k_s] \nabla \phi\} + q = F \frac{\partial \phi}{\partial t} \quad (7)$$

This work uses Equation 7. Different expressions for $k_r(h)$ and $\theta(h)$ are used as these are empirically based.

(ξ, η, ζ) equations

The approach taken is to first map a region of geometry into a (ξ, η, ζ) curvilinear coordinate system. For example, Figure 18 shows three surfaces of a circular region of soil around a well (O type grid in 3-D) that is mapped into a square box grid in the (ξ, η, ζ) system as shown in Figure 19. The inner cylinder at the well and the outer cylinder at the radius of influence are $\eta = \text{constant}$ surfaces, and the horizontal grid at the bottom plotted using thick lines is a $\zeta = \text{constant}$ surface.

Let J be the determinant of the transformation matrix between the two coordinate systems for a nonmoving grid as follows:

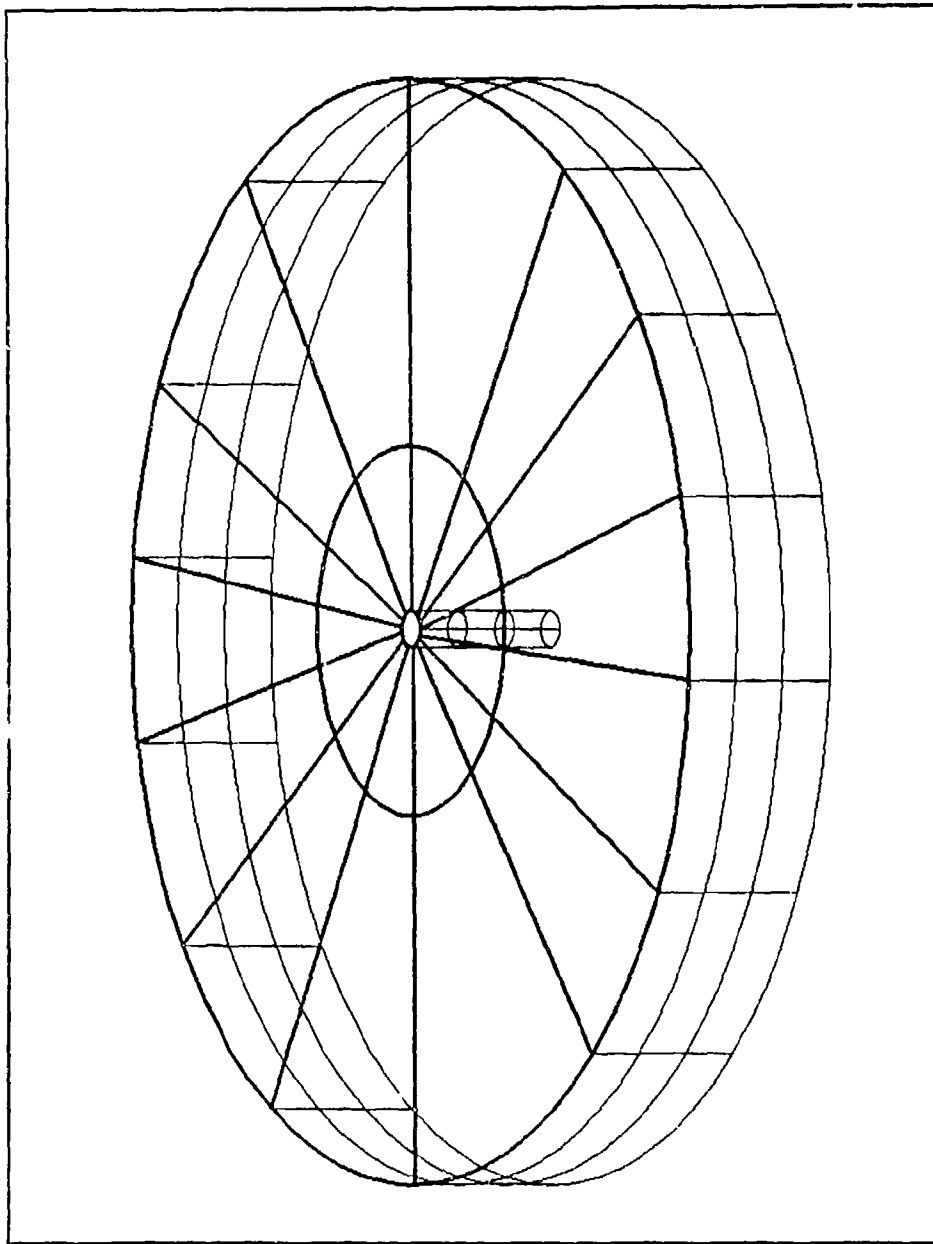


Figure 18. O grid

$$J = \begin{vmatrix} \frac{\partial x}{\partial \xi} & \frac{\partial y}{\partial \xi} & \frac{\partial z}{\partial \xi} \\ \frac{\partial x}{\partial \eta} & \frac{\partial y}{\partial \eta} & \frac{\partial z}{\partial \eta} \\ \frac{\partial x}{\partial \zeta} & \frac{\partial y}{\partial \zeta} & \frac{\partial z}{\partial \zeta} \end{vmatrix} \quad (8)$$

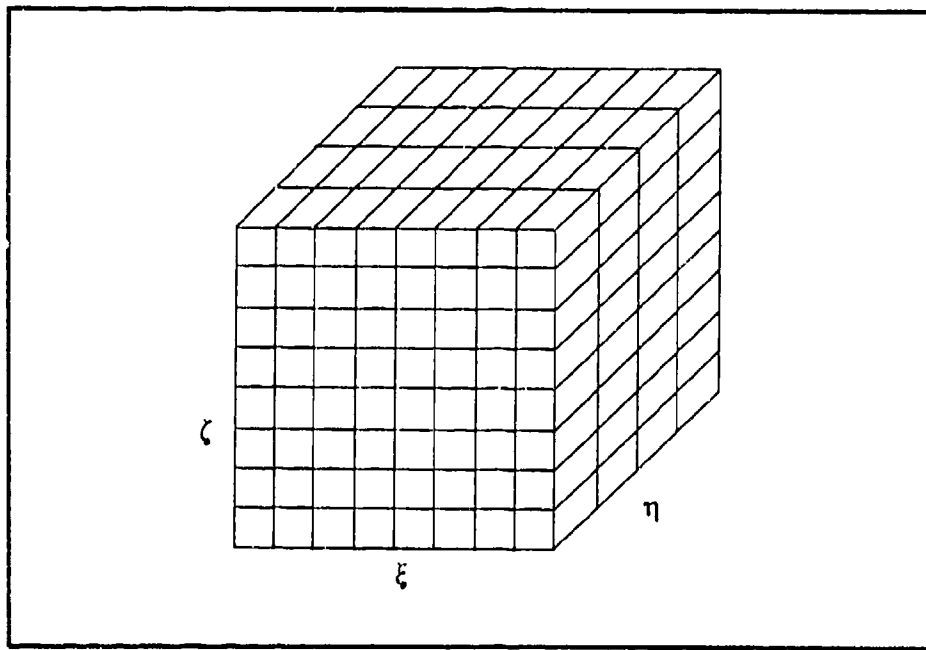


Figure 19. Square box grid

Appendix A contains derivations for certain equations in the curvilinear coordinate system. Using Equation A16 for the strong conservative form of the divergence of some vector $\{F\}$, we have

$$\begin{aligned}
 J\nabla^T\{F\} &= \frac{\partial}{\partial \xi} \left(J\nabla \xi^T\{F\} \right) + \frac{\partial}{\partial \eta} \left(J\nabla \eta^T\{F\} \right) + \frac{\partial}{\partial \zeta} \left(J\nabla \zeta^T\{F\} \right) \\
 &= \sum_{i=1}^3 \frac{\partial}{\partial \xi_i} \left(J\nabla \xi_i^T\{F\} \right)
 \end{aligned} \tag{9}$$

where ξ_i , $i = 1, 2, 3$ represent ξ , η , and ζ , respectively. Equation 9 applied to Equation 7 produces

$$\sum_{i=1}^3 \frac{\partial}{\partial \xi_i} \left(\nabla \xi_i^T \{k_r[k_s] J\nabla \phi\} \right) + Jq = JF \frac{\partial \phi}{\partial t} \tag{10}$$

Equation A12 can now be applied to the gradient of the potential to produce

$$\sum_{i=1}^3 \sum_{j=1}^3 \frac{\partial}{\partial \xi_i} \left(\nabla \xi_i^T \left\{ k_r[k_s] \frac{\partial}{\partial \xi_j} (J\nabla \xi_j) \right\} \right) + Jq = F \frac{\partial (J\phi)}{\partial t} \tag{11}$$

Finally, using the substitution

$$\Phi = J\varphi \quad (12)$$

in Equation 11, the following final result is obtained:

$$\sum_{i=1}^3 \sum_{j=1}^3 \frac{\partial}{\partial \xi_i} \left(\nabla \xi_i^T \left\{ k_r [k_s] \frac{\partial}{\partial \xi_j} (\Phi \nabla \xi_j) \right\} \right) + Jq = F \frac{\partial \Phi}{\partial t} \quad (13)$$

Equation 13 is the equation used in this FVM research.

Computational Procedure

There are enormous varieties of computational techniques that can be investigated for the solution of Equation 13. This effort can only choose some of the most promising techniques and investigate them. The chosen solution will now be presented, and for simplicity, a 2-D formulation is given.

Finite volume cell

The standard FV strategy is to consider each computational cell an FV with the unknown variables to be computed evaluated at the center of the cell. However, the FEM usually has the value of the unknowns computed at the grid points (node points). So, as shown in Figure 20, a modified way of defining the finite volumes (McCormick 1992) is to use the dotted

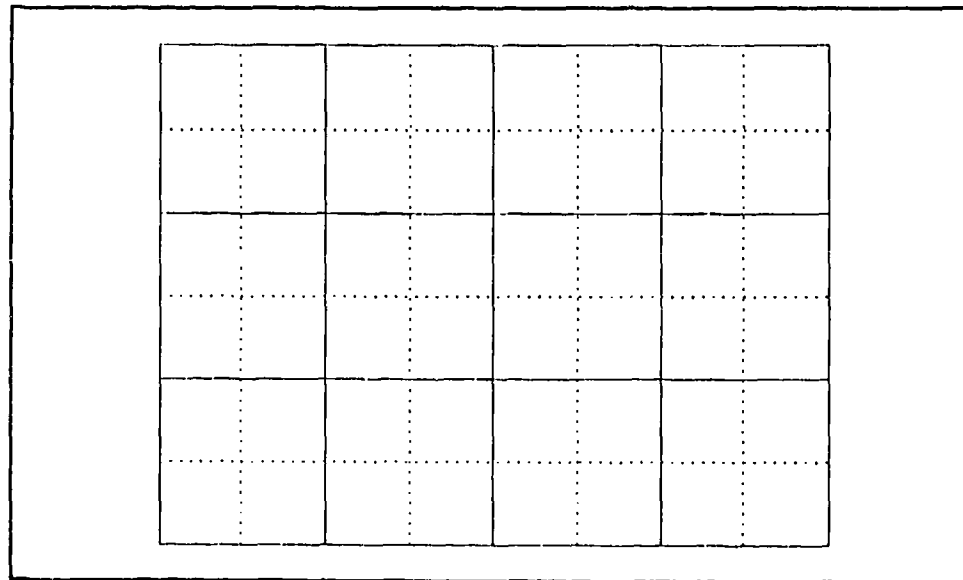


Figure 20. 2-D computational grid

lines to form cells around the node points. This has the advantage of allowing the identical grid to be used for FEM or FVM, but a disadvantage is the cells along the boundary have reduced size by one-half or one-fourth. This problem has, however, been minimized by a judicious software design of subroutines.

Discretized equation

To understand how Equation 13 is discretized, first consider the simpler equation

$$\frac{\partial p}{\partial \xi} + \frac{\partial q}{\partial \eta} = \frac{\partial r}{\partial t} \quad (14)$$

where p , q , and r are each some continuous function. Let each computational area be a unit square. Also, an implicit formulation is sought at time $t = (n + 1)\Delta t$ with an Euler approximation to the time partial derivative. Then, multiplying Equation 14 by $d\xi d\eta$ and integrating over the unit square of a node at grid point (i, j) gives

$$f_{i+\frac{1}{2},j}^{n+1} - f_{i-\frac{1}{2},j}^{n+1} + g_{i,j+\frac{1}{2}}^{n+1} - g_{i,j-\frac{1}{2}}^{n+1} = \frac{h_{i,j}^{n+1} - h_{i,j}^n}{\Delta t} \quad (15)$$

where the one-half designations represent evaluation of information on the respective edges of the finite volume cell. Traditionally, it is stated that the value at the node point (center of the cell) is taken as the constant value over the entire cell, and that is why the integral signs can vanish. However, a better interpretation is that the value at the node point represents the average value of the variable over the cell. In like manner, rather than thinking of the one-half terms as being constant on the line segments, the only restraint required is that this value represent the average value on its corresponding line segment.

This same process can now be applied to a 2-D version of Equation 13 to obtain

$$\begin{aligned}
& \left(\nabla \xi^T \left\{ k_r [k_s] \frac{\partial}{\partial \xi} (\Phi \nabla \xi) \right\} \right)_{i+\frac{1}{2},j}^{n+1} \\
& - \left(\nabla \xi^T \left\{ k_r [k_s] \frac{\partial}{\partial \xi} (\Phi \nabla \xi) \right\} \right)_{i-\frac{1}{2},j}^{n+1} \\
& + \left(\nabla \xi^T \left\{ k_r [k_s] \frac{\partial}{\partial \eta} (\Phi \nabla \eta) \right\} \right)_{i+\frac{1}{2},j}^{n+1} \\
& - \left(\nabla \xi^T \left\{ k_r [k_s] \frac{\partial}{\partial \eta} (\Phi \nabla \eta) \right\} \right)_{i-\frac{1}{2},j}^{n+1} \\
& + \left(\nabla \eta^T \left\{ k_r [k_s] \frac{\partial}{\partial \xi} (\Phi \nabla \xi) \right\} \right)_{i,j+\frac{1}{2}}^{n+1} \\
& - \left(\nabla \eta^T \left\{ k_r [k_s] \frac{\partial}{\partial \xi} (\Phi \nabla \xi) \right\} \right)_{i,j-\frac{1}{2}}^{n+1} \\
& + \left(\nabla \eta^T \left\{ k_r [k_s] \frac{\partial}{\partial \eta} (\Phi \nabla \eta) \right\} \right)_{i,j+\frac{1}{2}}^{n+1} \\
& - \left(\nabla \eta^T \left\{ k_r [k_s] \frac{\partial}{\partial \eta} (\Phi \nabla \eta) \right\} \right)_{i,j-\frac{1}{2}}^{n+1} \\
& + Jq = F_{i,j}^{n+1} \frac{\Phi_{i,j}^{n+1} - \Phi_{i,j}^n}{\Delta t}
\end{aligned} \tag{16}$$

Let the remaining partial derivatives in Equation 16 be approximated by central differences. Then the first term of Equation 16 becomes

$$\begin{aligned}
T_1 &= \left(\nabla \xi^T \left\{ k_r [k_s] \frac{\partial}{\partial \xi} (\Phi \nabla \xi) \right\} \right)_{i+\frac{1}{2},j}^{n+1} \\
&= \left(\nabla \xi^T k_r [k_s] \right)_{i+\frac{1}{2},j}^{n+1} \left\{ \nabla \xi_{i+1,j} \Phi_{i+1,j}^{n+1} - \nabla \xi_{i,j} \Phi_{i,j}^{n+1} \right\}
\end{aligned} \tag{17}$$

And the third term of Equation 16 is now

$$\begin{aligned}
 T_3 &= \left(\nabla \xi \left\{ k_r [k_s] \frac{\partial}{\partial \eta} (\Phi \nabla \eta) \right\} \right)_{i+\frac{1}{2},j}^{n+1} \\
 &= \frac{1}{2} \left(\nabla \xi^T k_r [k_s] \right)_{i+\frac{1}{2},j}^{n+1} \left\{ \nabla \eta_{i+1,j+1} \Phi_{i+1,j+1}^{n+1} \right. \\
 &\quad \left. - \nabla \eta_{i+1,j-1} \Phi_{i+1,j-1}^{n+1} \right\}
 \end{aligned} \tag{18}$$

Define the terms

$$\begin{aligned}
 \{A^+\}^T &= \left(\nabla \xi^T k_r [k_s] \right)_{i+\frac{1}{2},j}^{n+1} \\
 \{A^-\}^T &= \left(\nabla \xi^T k_r [k_s] \right)_{i-\frac{1}{2},j}^{n+1} \\
 \{B^+\}^T &= \left(\nabla \eta^T k_r [k_s] \right)_{i,j+\frac{1}{2}}^{n+1} \\
 \{B^-\}^T &= \left(\nabla \eta^T k_r [k_s] \right)_{i,j-\frac{1}{2}}^{n+1}
 \end{aligned} \tag{19}$$

Then Equation 16 becomes

$$\sum_{m=-1}^1 \sum_{n=-1}^1 C_{i+m,j+n}^{n+1} \Phi_{i,j}^{n+1} = -Jq - \frac{1}{\Delta t} F_{i,j}^{n+1} \Phi_{i,j}^n \tag{20}$$

where the C 's are coefficients that are still functions of the dependent variable, and thus Equation 20 remains a nonlinear equation. Nevertheless, the C 's in a nine-point template format are given in Table 2.

Computation of geometric quantities

The geometric quantities can be computed in a variety of ways. Each element (Figure A1) is treated as a four-node isoparametric element. Thus, the transformation between x and (ξ, η) becomes

| Table 2 Nine-Point Template | | | |
|--------------------------------|---|--|---|
| 1 | $-\frac{\{A^-\}^T \nabla \eta}{2}$ $-\frac{\{B^+\}^T \nabla \xi}{2}$ | $\{B^+\}^T \nabla \eta$ | $+\frac{\{A^+\}^T \nabla \eta}{2}$ $+\frac{\{B^+\}^T \nabla \xi}{2}$ |
| 0 | $\{A^-\}^T \nabla \xi$ | $-\{A^+ + A^-\}^T \nabla \xi$ $-\{B^+ + B^-\}^T \nabla \eta$ $-\frac{1}{\Delta t} F^{n+1}$ | $\{A^+\}^T \nabla \xi$ |
| -1 | $+\frac{\{A^-\}^T \nabla \eta}{2}$ $+\frac{\{B^-\}^T \nabla \xi}{2}$ | $\{B^-\}^T \nabla \eta$ | $-\frac{\{A^+\}^T \nabla \eta}{2}$ $-\frac{\{B^-\}^T \nabla \xi}{2}$ |
| n_m | -1 | 0 | 1 |

$$x = (\xi_0 + 1 - \xi) (\eta_0 + 1 - \eta) x_1 + (\xi - \xi_0) (\eta_0 + 1 - \eta) x_2 \\ + (\xi - \xi_0) (\eta - \eta_0) x_3 + (\xi_0 + 1 - \xi) (\eta - \eta_0) x_4 \quad (21)$$

where

(ξ_0, η_0) = integer values of the computational coordinates for the first node of the computational element

x_1, x_2, x_3 , and x_4 = x coordinates at the node points

A similar expression to Equation 21 exists for y . Terms like

$$\frac{\partial x}{\partial \xi} = -(\eta_0 + 1 - \eta) x_1 + (\eta_0 + 1 - \eta) x_2 \\ + (\eta - \eta_0) x_3 - (\eta - \eta_0) x_4 \quad (22)$$

can now be computed using Equation 21. Evaluating Equation 22 at the center of the computational element yields

$$\left(\frac{\partial x}{\partial \xi} \right)_c = \frac{1}{2} (x_2 - x_1 + x_3 - x_4) \quad (23)$$

Values at the node points are computed by averaging the surrounding center values (four for internal nodes) using Equation 23. Finally, J , $\nabla \xi$, and $\nabla \eta$ are computed using Equations A4, A6, and A7. Matrices such as those in Equation 19 are first evaluated at the nodes and then averaged to find values for the sides.

Nonlinear Iteration

Although terms in Equation 20 can now be computed, Equation 20 is still nonlinear, so some iteration scheme must be adopted. Different schemes were considered, including the Picard and Newton schemes (Putti and Paniconi 1992). Presented here is the scheme that worked well for the problems tested.

Modified Newton scheme. Given a nonlinear equation

$$f(\Phi) = 0 \quad (24)$$

but at the k 'th iteration

$$f(\Phi^k) \neq 0 \quad (25)$$

then a Taylor Series expansion can be used as follows:

$$f(\Phi^{k+1}) = f(\Phi^k) + \left(\frac{\partial f}{\partial \Phi} \right)_k \Delta \Phi + \dots \quad (26)$$

So a first-order approximation is to set the right-hand part of Equation 26 to zero to yield

$$\Delta \Phi = - \frac{f(\Phi^k)}{\left(\frac{\partial f}{\partial \Phi} \right)_k} \quad (27)$$

Now, apply Equation 27 to

$$\begin{aligned} f(\Phi^{k+1}) = & \sum_{m=-1}^1 \sum_{n=-1}^1 C_{i+m,j+n}^{k+1} \Phi_{i+m,j+n}^{k+1} + Jq \\ & + \frac{1}{\Delta t} F_{i,j}^{k+1} \Phi_{i,j}^k \end{aligned} \quad (28)$$

(from Equation 20) in such a way as to neglect the partial derivatives of C and F to obtain

$$\sum_{m=-1}^1 \sum_{n=-1}^1 C_{i+m,j+n}^k \Delta\Phi_{i+m,j+n}^{k+1} = -f(\Phi^k) \quad (29)$$

Solution of equations. Equation 29 can be solved by any number of direct or iterative techniques, such as forms of Gauss Elimination or the preconditioned conjugate gradient method. The unknown variables then can be updated with the process continuing until the updates become so small that the solution for the current time-step has converged. However, an under-relaxation type method (the conjugate gradient method will be tested later) worked well enough for the problems tested. Because of the nonlinearity, first the Gauss-Seidel type computation

$$\Delta\Phi_{i,j}^{k+1} = \frac{1}{C_{i,j}^k} \left(-f(\Phi^k) - \sum_{m=-1}^1 \sum_{n=-1}^1 C_{i+m,j+n}^k \Delta\Phi_{i,j}^k + C_{i,j}^k \Delta\Phi_{i,j}^k \right) \quad (30)$$

was performed. Then, after results for all nodes have been done, update using

$$\Phi_{i,j}^{k+1} = \Phi_{i,j}^k + \alpha \Delta\Phi_{i,j}^{k+1} \quad (31)$$

where α varies between zero and 1. Equations 30 and 31 can be executed several times before updating the C 's and F , but it was more efficient to update all data after each iteration. Since only scalar operations are done, each iteration is very fast. Of course, more iterations will be required, so only a partial payoff is realized.

Test Problems

Two test problems will now be given to show the effectiveness of the solution presented. Comparison with FEM results will also be made.

Dupuit's problem

The first problem is the classic problem of steady state, unconfined flow in an earth embankment with vertical sides and an impervious base as shown in Figure 21. Water flows from headwater to the exit face where the pressure = 0 line represents the free surface. The embankment is 100 by 100 ft (30.48 m), the headwater level is at 100 ft, and the tailwater is at 20 ft (6.096 m). The exit point where the free surface intersects the downstream vertical boundary is 40 ft (12.192 m). A grid of $11 \times 11 = 121$ nodes

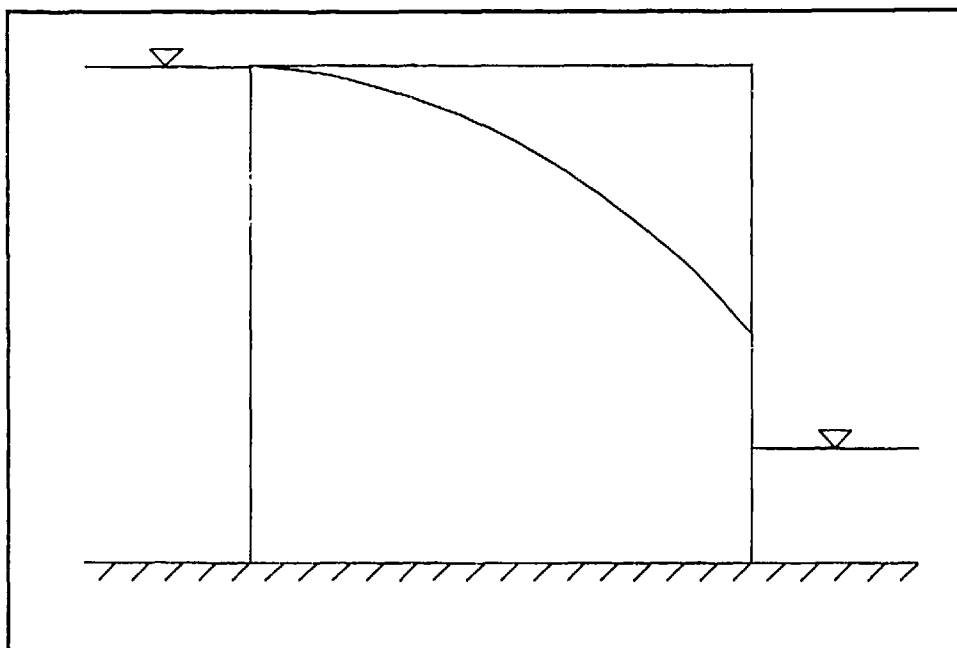


Figure 21. Dupuit's problem

and $10 \times 10 = 100$ elements with $\Delta x = 10$ ft (3.048 m) and $\Delta y = 10$ ft (3.048 m) was built and run on the developed FV program and a 2-D saturated, confined/unconfined flow FEM program. Again, because of the way the FV program was constructed, the identical grid and boundary conditions can be used in both codes.

The 2-D FEM program (2DSEEP) computes "stiffness" type matrices and then assembles them to form the set of equations to be solved. These stiffness matrices are numerically integrated by evaluating the integrand at certain integration points and then using a Gauss quadrature formula. Typically, $2 \times 2 = 4$ integration points are used, but because the free surface can go through an element, 2DSEEP uses $4 \times 4 = 16$ integration points. The relative hydraulic conductivity is then set to 0.001 for an integration point with pressure head of less than zero. This integration provides a smearing process so the transition is not so abrupt.

Since no integration is used in the FV algorithm, a 5-ft (1.524-m) transition zone was therefore provided where the relative hydraulic conductivity varied from 1 to 0.001 when the pressure head varied from 0 to -5 ft (-1.524 m). Relative hydraulic conductivity was then kept at 0.001 for all values of pressure head less than -5 ft (-1.524 m).

Finally, the moisture capacity F in Equation 5 is set to zero to eliminate the time-dependent aspect of Equation 4 for a steady-state solution.

Figure 22 shows a comparison of the free surface for the FEM and FV solutions. Note that they are rather close. Also, the running times of the two solutions can be compared. It must be emphasized that the FEM

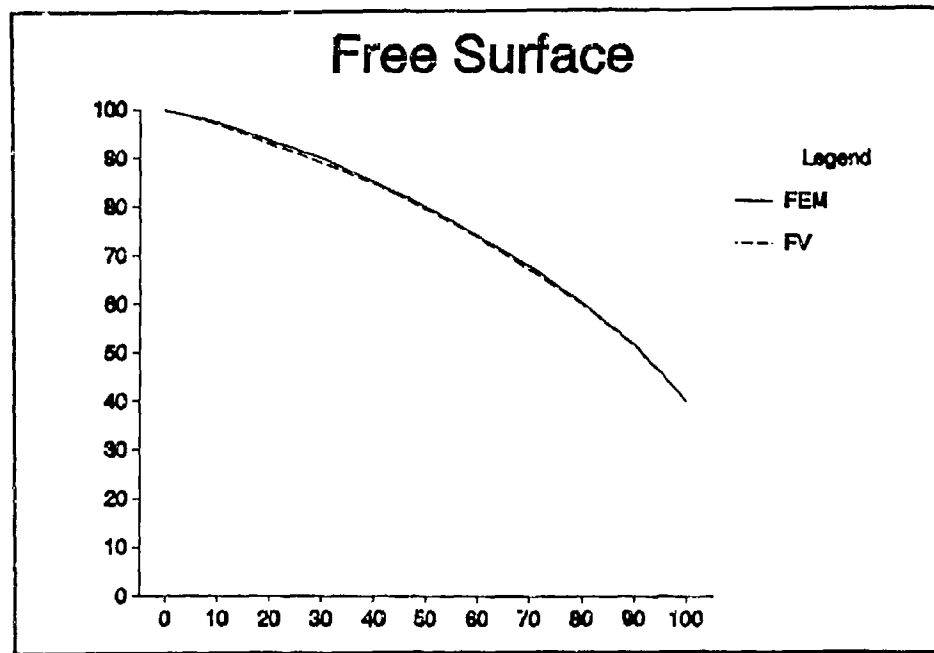


Figure 22. Comparison of FEM and FV free surface

technique has significantly more computations because of the numerical integration process and the solution of a banded system of equations at each iteration. In general, fewer elements for the FEM solution are therefore needed compared to the FV grid. Also, because a banded system is solved compared to a relaxation iteration, much fewer FEM iterations are needed. With these thoughts in mind, the FEM solution took 1 min, 13 sec, and seven iterations on a 486 class PC running at 33 mhz, and the FV solution took 12 sec with 124 iterations. It should also be observed that the diagonal terms in the template in Table 2 go to zero for this square grid, making the formulation similar to a standard finite difference algorithm.

Laboratory test problem

Results from an experimental study of 2-D transient unsaturated/saturated flow with water table recharge (Vauclin, Khanji, and Vachaud 1979) will now be compared with results from both the FV formulation and a 3-D transient unsaturated/saturated FEM flow code. The problem, as shown in Figure 23, consists of flow in a homogeneous soil of saturated hydraulic conductivity 35 cm/hr in a tank 600 cm long, 200 cm tall, and 5 cm thick with an impervious bottom. Because of symmetry, only 300 cm of the tank are modeled with the center line (AF in Figure 23) being treated as an impervious boundary. A constant pool elevation of 65 cm is maintained along BC in Figure 23 with the boundary CDE covered to avoid evaporation. EF is initially covered and the tank is allowed to completely settle. Then EF is uncovered and a flow rate of 14.8 cm/hr is applied to the system for 8 hr while holding BC at the constant total head of 65 cm.

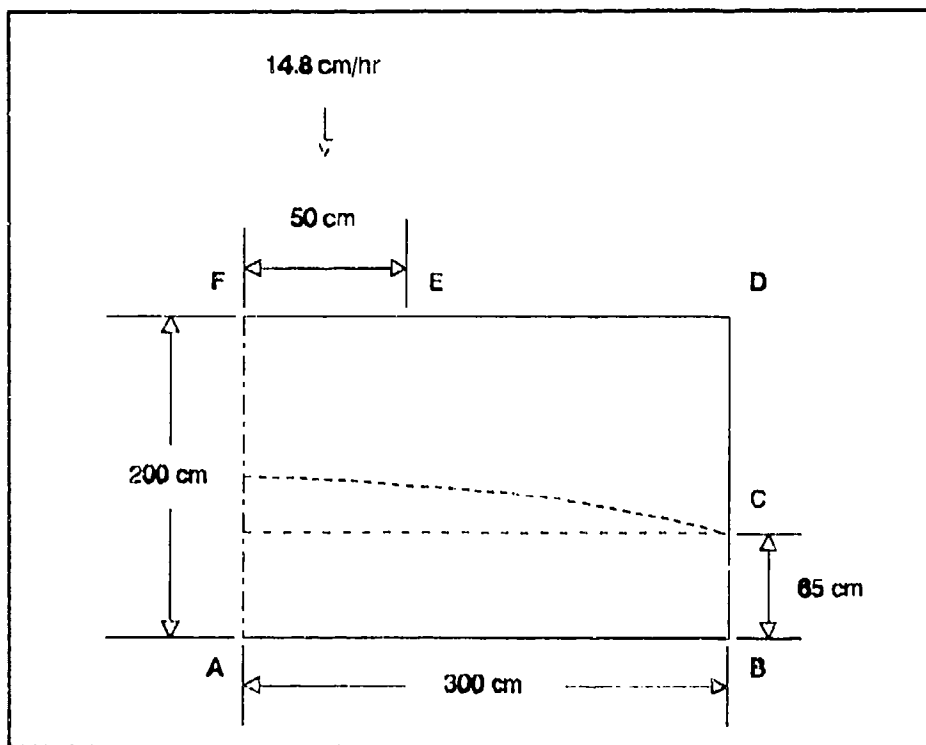


Figure 23. Laboratory problem

The relative hydraulic conductivity in the unsaturated region was determined experimentally to be

$$k_r = \frac{A}{A + (-h)^B} \quad (32)$$

where

$$A = 2.99 \times 10^6$$

$$B = 5.0$$

The moisture content equation was also determined experimentally and by the use of a least-squares fit to be

$$\theta = \theta_s \frac{\alpha}{\alpha + (-h)^\beta} \quad (33)$$

where

$$\theta_s = 0.30$$

$$\alpha = 40.00$$

$$\beta = 2.90$$

The grid (shown in Figure 24) consists of a 16×16 structured grid with the intervals slightly different to align with key points. For example, the dot is a node at (161, 79) where pressure head data were collected. Δt was set to 0.05 hr and allowed to grow 20 percent a time-step until a maximum of $\Delta t = 1$ hr was reached. Twenty time-steps were done for a total of 8 hr. The proper subroutine was modified to incorporate Equations 32, 33, and the derivative of Equation 33 (from Equation 5), and the problem was run on both the FEM and FV codes. Because of the nature of the water capacity curve (Figure 25), the FEM program would not converge, and the FV solution converged only by using a small $\alpha = 0.1$ in Equation 31 for the first few time-steps. The FEM algorithm uses a Picard-type iteration strategy, while the FV scheme uses the Newton-type iteration as previously described. However, tabular forms of Equations 32, 33, and F (27 data points), with F not allowed smaller than 0.001 for large $-h$, were used with the FEM code, and convergence was then achieved. A Picard-type algorithm was implemented in the FV code, and the same lack of convergence was observed. Newton-versus-Picard iteration is an important research topic, so at least for this problem and implementation, the Newton algorithm is superior.

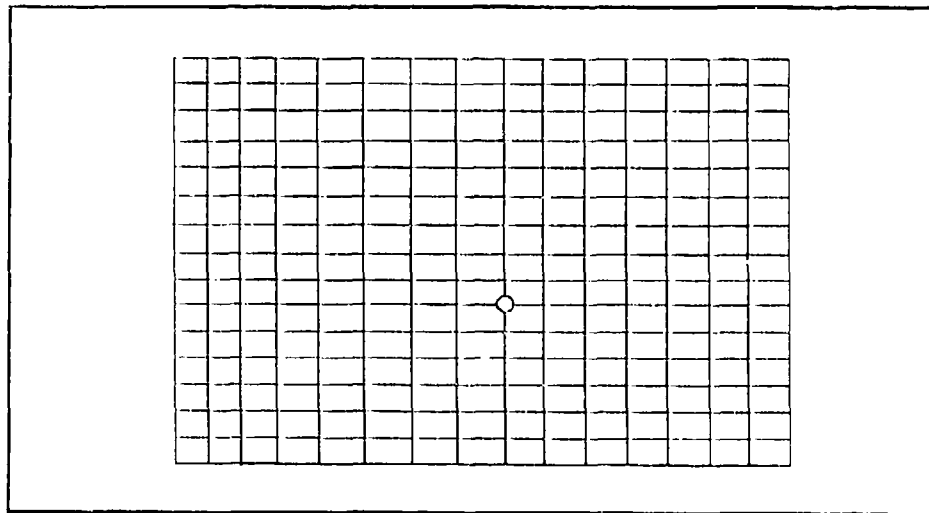


Figure 24. Grid

The results for the 40 time-steps for both the FV and FEM solutions were then obtained, and the free surface was compared with the laboratory results as shown in Figure 26. The dissipative error in the FEM solution is more than that of the FV implementation. F being modeled more accurately in the FV code could have had an impact as well.

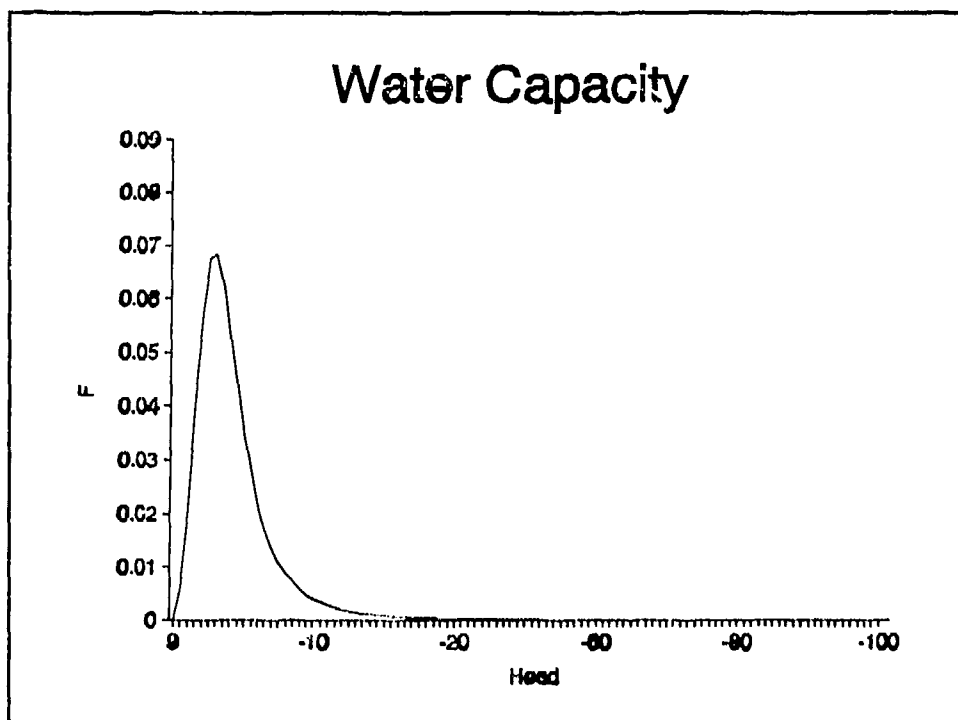


Figure 25. Water capacity curve

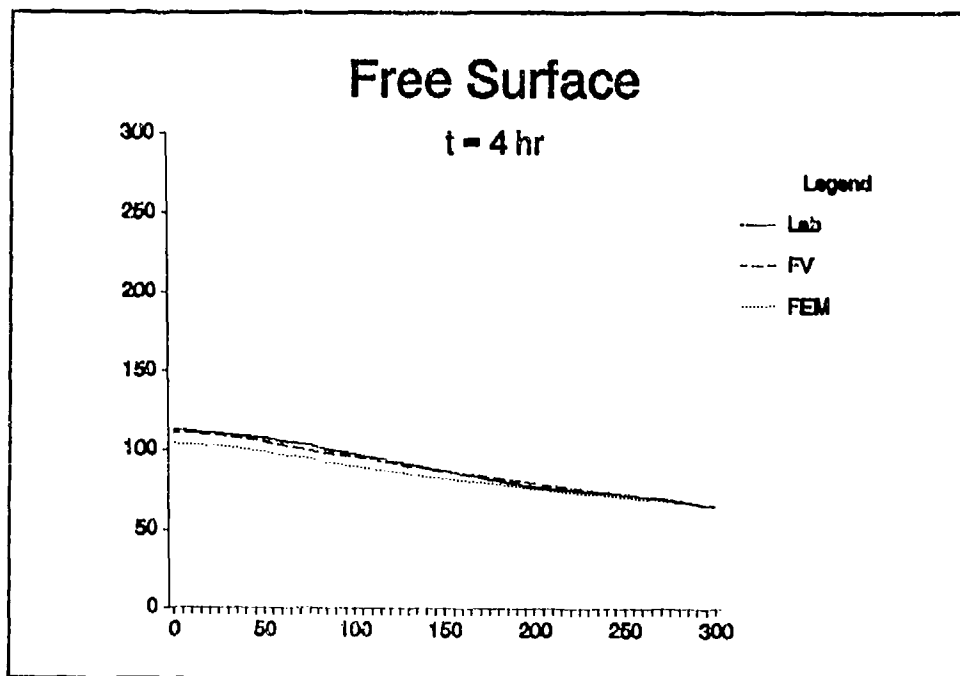


Figure 26. Comparison of laboratory, FEM, and FV results

Summary and Conclusions

There are many more problems that can be considered in unsaturated flow. There are problems with difficult geometries and heterogeneities. In some cases, the FEM will function better, and in other cases, as has been demonstrated, the FVM will function better. But it can be concluded on the basis of this study that alternative techniques such as the FVM can be a powerful tool for groundwater modeling.

4 Contaminant Transport

Introduction

Chapter 3 showed the application of the FVM to unsaturated flow with good results. This chapter will investigate the effectiveness of the FVM for contaminant transport. There are several higher-order numerical techniques with one being the Lagrangian-Eulerian Method (LEM) (Yeh 1990). This technique has almost exclusively been used with the FEM, so this chapter shows the results of R&D using both FVM and LEM. The following will be presented:

- a. *Governing equations.* The equations used in this work to model contaminant transport, including the one used for the LE approach.
- b. *Computational procedure.* The LE algorithm in an FV environment.
- c. *Comparison of results.* Results obtained from this FVM technique are compared with FEM results for analytical solutions.

Governing Equations

The governing partial differential equation for contaminant transport in unsaturated porous media at a given (x, y, z) point in space and time t is

$$\frac{\partial(\theta C)}{\partial t} + \rho_b \frac{\partial S}{\partial t} + \nabla \cdot (\nu C) = \nabla \cdot (\theta D \cdot \nabla C) - \lambda(\theta C + \rho_b S) + Q C_{in} \quad (34)$$

where

θ = moisture content

C = material concentration in aqueous phase (ML^{-3})

ρ_b = bulk density of the medium

S = material concentration in adsorbed phase (M/M)

\mathbf{v} = discharge velocity vector

\mathbf{D} = dispersion coefficient tensor

λ = decay constant

Q = source rate of water

C_{in} = material concentration in the source

For this study, the linear isotherm model for adsorption is used, which is

$$S = K_d C \quad (35)$$

where K_d is the distribution coefficient

The ij 'th component of the dispersion coefficient tensor d_{ij} is given by

$$d_{ij} = \frac{1}{\theta} \left(a_T |\mathbf{v}| \delta_{ij} + (a_L - a_T) \frac{v_i v_j}{|\mathbf{v}|} \right) + a_m \tau \delta_{ij} \quad (36)$$

where

a_T = lateral dispersivity

a_L = longitudinal dispersivity

v_i = i 'th component of \mathbf{v}

a_m = molecular diffusion coefficient

τ = tortuosity

and

$$\begin{aligned} \delta_{ij} &= 1 & i &= j \\ &= 0 & i &\neq j \end{aligned} \quad (37)$$

Equation 34 can be expanded and combined with Equation 35 to produce

$$\begin{aligned} (\theta + \rho_b K_d) \frac{\partial C}{\partial t} + \mathbf{v} \cdot \nabla C + \left(\frac{\partial \theta}{\partial t} + \nabla \cdot \mathbf{v} \right) C \\ = \nabla \cdot (\theta \mathbf{D} \cdot \nabla C) - \lambda (\theta + \rho_b K_d) C + Q C_{in} \end{aligned} \quad (38)$$

Also, unsaturated flow is modeled by

$$\frac{\partial \theta}{\partial t} + \nabla \cdot \mathbf{v} = Q \quad (39)$$

Equations 38 and 39 can be combined to produce the following governing equation used in this study:

$$\begin{aligned} \left(\theta + \rho_b K_d \right) \frac{\partial C}{\partial t} + \mathbf{v} \cdot \nabla C = \nabla \cdot (\theta \mathbf{D} \cdot \nabla C) \\ - \left[\lambda \left(\theta + \rho_b K_d \right) + Q \right] C + Q C_{in} \end{aligned} \quad (40)$$

Eulerian Versus Lagrangian Approach

The typical approach in 2-D is to stay at a given (x, y) position in space and observe phenomena as they pass. This is known as the Eulerian system and is represented by Equation 40. Another approach is to have the observation point move as well at the same velocity as the particles of fluid (Lagrangian system). The Eulerian approach is modeled using a fixed grid, and the Lagrangian approach can be handled using a moving grid with each node point moving at their respective velocities. This can lead to a skewed grid after a while, so a modified approach (LEM) is used in this study.

Using the chain rule of differentiation, the change of concentration for a node in a moving grid is given by

$$\left(\frac{\partial C}{\partial t} \right)_{gp} = \left(\frac{\partial C}{\partial t} \right)_{fp} + \left(\frac{\partial C}{\partial x} \right) v_x + \left(\frac{\partial C}{\partial y} \right) v_y \quad (41)$$

where the subscript gp represents grid point, the subscript fp represents a fixed (x, y) point in space, v_x is the speed of the grid point in the x direction, and v_y is the speed of the grid point in the y direction. The first time derivative is often written with a capital D , and the second time derivative is what appears in Equation 40, so rewrite Equation 41 as

$$\frac{DC}{Dt} = \frac{\partial C}{\partial t} + \mathbf{v} \cdot \nabla C \quad (42)$$

where \mathbf{v} = grid point velocity vector

Equation 42 can now be substituted into Equation 40 to get

$$\begin{aligned}
& \left(\theta + \rho_b K_d \right) \left[\frac{DC}{Dt} + \left(\frac{v}{\theta + \rho_b K_d} - v \right) \cdot \nabla C \right] \\
& = \nabla \cdot (\theta D \cdot \nabla C) - \left[\lambda (\theta + \rho_b K_d) + Q \right] C + QC_{in}
\end{aligned} \tag{43}$$

So if the velocity of the grid point is

$$v = \frac{v}{\theta + \rho_b K_d} \tag{44}$$

then the Lagrangian equation representing contaminant transport becomes

$$\begin{aligned}
& \left(\theta + \rho_b K_d \right) \frac{DC}{Dt} = \nabla \cdot (\theta D \cdot \nabla C) \\
& - \left[\lambda (\theta + \rho_b K_d) + Q \right] C + QC_{in}
\end{aligned} \tag{45}$$

Computational Procedure

It must be emphasized that the resulting concentrations from Equation 45 are for a grid that has moved. Therefore, the following two steps must be performed in either order:

- a. *Lagrangian.* Compute an advection contribution using grid point speeds according to Equation 44.
- b. *Eulerian.* Compute dispersion and other contributions using Equation 45.

In this work the advection step is first.

Lagrangian step

The FV transport code that was written for this research takes as input the moisture content and discharge velocity for each node and each time-step. Therefore, for a given node P (as shown in Figure 27 where both the velocity components are positive), grid speed velocities at time-step n can be computed by

$$v^n = \frac{v^n}{\theta^n + \rho_b K_d} \tag{46}$$

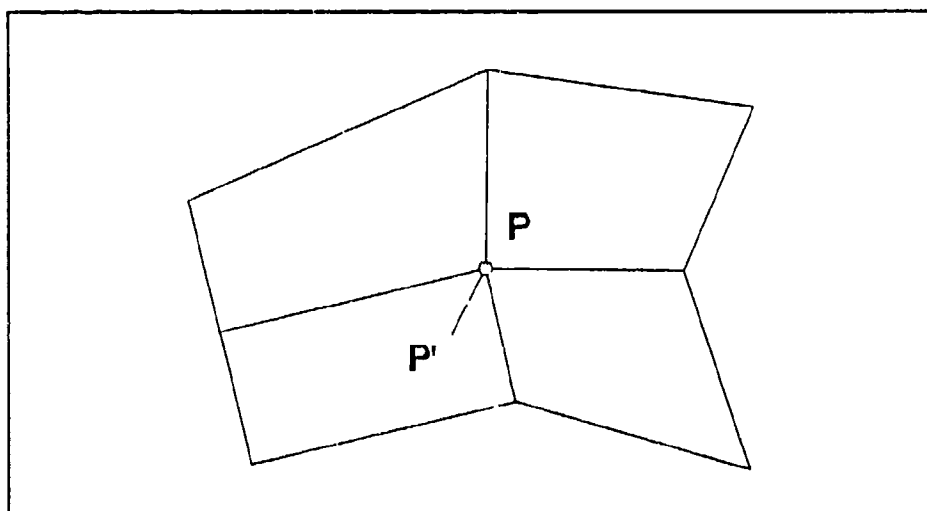


Figure 27. Grid point

The distance node point P travels during a time-step Δt is

$$\Delta r = \frac{1}{2} (v^n + v^{n+1}) \Delta t \quad (47)$$

Now if the approximation is made that point P' travels the same Δr to reach point P for the time interval Δt (backward tracking), then the advection concentration C^* at time $n+1$ for node P is simply the concentration at P' . However, the grid velocity at P' is not in general the same as it is at P , leading to possible error. A correcting formulation follows.

Computation of C^* at P' . As before, assume a four-point isoparametric finite element formulation for each cell as shown in Figure A1, except that now let the parameters ξ, η vary between 0 and 1. Then inside each element

$$\begin{aligned} \begin{Bmatrix} x \\ y \\ C \\ v \end{Bmatrix} &= (1 - \xi)(1 - \eta) \begin{Bmatrix} x \\ y \\ C \\ v \end{Bmatrix}_1 + \xi(1 - \eta) \begin{Bmatrix} x \\ y \\ C \\ v \end{Bmatrix}_2 \\ &\quad + \xi\eta \begin{Bmatrix} x \\ y \\ C \\ v \end{Bmatrix}_3 + (1 - \xi)\eta \begin{Bmatrix} x \\ y \\ C \\ v \end{Bmatrix}_4 \end{aligned} \quad (48)$$

The more accurate equation for r' , the position of P' , using Equation 47 is

$$\frac{1}{2} (v^n + v^{n+1}) \Delta t = r_p - r' \quad (49)$$

where

$v' =$ grid speed at P'

$r_p =$ vector containing the (x, y) coordinates of point P

For the i 'th node of the cell, define the quantities

$$R_i = \begin{Bmatrix} X \\ Y \end{Bmatrix}_i = r_i + \frac{1}{2} (v_i^n + v_i^{n+1}) \Delta t \quad (50)$$

Applying Equation 48 to the prime variables in Equation 49, using the definition of Equation 50, and collecting terms yields a set of equations to calculate (ξ', η') as follows:

$$\begin{aligned} (X_1 - X_2 + X_3 - X_4) \xi' \eta' + (X_2 - X_1) \xi' \\ + (X_4 - X_1) \eta' = x_p - X_1 \end{aligned} \quad (51)$$

$$\begin{aligned} (Y_1 - Y_2 + Y_3 - Y_4) \xi' \eta' + (Y_2 - Y_1) \xi' \\ + (Y_4 - Y_1) \eta' = y_p - Y_1 \end{aligned}$$

Rewrite these equations using constants $a_1, a_2, b_1, b_2, c_1, c_2, d_1$, and d_2 as

$$\begin{aligned} a_1 \xi' \eta' + b_1 \xi' + c_1 \eta' &= d_1 \\ c_1 \eta' + b_2 \xi' + c_2 \eta' &= d_2 \end{aligned} \quad (52)$$

The first of these equations can be solved for η' to yield

$$\eta' = \frac{d_1 - b_1 \xi'}{c_1 + a_1 \xi'} \quad (53)$$

Equation 53 can now be substituted into the bottom portion of Equation 52 to obtain the quadratic equation

$$\begin{aligned} (a_1 b_2 - a_2 b_1) \xi'^2 - (a_1 d_2 + b_1 c_2 - c_1 b_2 \\ - d_1 a_2) \xi' - c_1 d_2 + d_1 c_2 = 0 \end{aligned} \quad (54)$$

which can now be easily solved for ξ' . This done, η' can be computed from Equation 53, and finally, substituting the values of ξ' and η' into the C row of Equation 48, the value of concentration at P' is given.

Determining what cell to locate P' . Figure 27 shows that when both components of grid speed are positive, the negative x and y direction is where the proper cell is. Since this FV formulation is on a structured grid, the process of finding the proper cell is to simply look in the four adjacent cells by solving Equation 51 for ξ' and η' and selecting the cell where ξ' and η' are both between 0 and 1.

Eulerian step

The final step is to use the C^* values in conjunction with an FV representation of Equation 45 to determine the concentration at each node. Since Equation 45 is remarkably similar to Equation 7, a very similar formulation can be used. With the definition

$$\Phi = JC \quad (55)$$

the curvilinear coordinate version of Equation 45 is

$$\begin{aligned} \sum_{i=1}^3 \sum_{j=1}^3 \frac{\partial}{\partial \xi_i} \left(\nabla \xi_i^T \left\{ \theta[D] \frac{\partial}{\partial \xi_j} (\Phi \nabla \xi_j) \right\} \right) - [\lambda(\theta + \rho_b K_d) + Q] \Phi \\ + JQC_{in} = (\theta + \rho_b K_d) \frac{D\Phi}{Dt} \end{aligned} \quad (56)$$

The FV representation is

$$\begin{aligned} \left(\nabla \xi^T \left\{ \theta[D] \frac{\partial}{\partial \xi} (\Phi \nabla \xi) \right\} \right)_{i+\frac{1}{2},j}^{n+1} - \left(\nabla \xi^T \left\{ \theta[D] \frac{\partial}{\partial \xi} (\Phi \nabla \xi) \right\} \right)_{i-\frac{1}{2},j}^{n+1} \\ + \left(\nabla \xi^T \left\{ \theta[D] \frac{\partial}{\partial \eta} (\Phi \nabla \eta) \right\} \right)_{i+\frac{1}{2},j}^{n+1} - \left(\nabla \xi^T \left\{ \theta[D] \frac{\partial}{\partial \eta} (\Phi \nabla \eta) \right\} \right)_{i-\frac{1}{2},j}^{n+1} \\ + \left(\nabla \eta^T \left\{ \theta[D] \frac{\partial}{\partial \xi} (\Phi \nabla \xi) \right\} \right)_{i,j+\frac{1}{2}}^{n+1} - \left(\nabla \eta^T \left\{ \theta[D] \frac{\partial}{\partial \xi} (\Phi \nabla \xi) \right\} \right)_{i,j-\frac{1}{2}}^{n+1} \\ + \left(\nabla \eta^T \left\{ \theta[D] \frac{\partial}{\partial \eta} (\Phi \nabla \eta) \right\} \right)_{i,j+\frac{1}{2}}^{n+1} - \left(\nabla \eta^T \left\{ \theta[D] \frac{\partial}{\partial \eta} (\Phi \nabla \eta) \right\} \right)_{i,j-\frac{1}{2}}^{n+1} \\ - \left(\lambda \alpha_{i,j}^{n+1} + Q \right) \Phi_{i,j}^{n+1} + JQC_{in} = \alpha_{i,j}^{n+1} \frac{\Phi_{i,j}^{n+1} - \Phi_{i,j}^*}{\Delta t} \end{aligned} \quad (57)$$

where

$$\alpha_{i,j}^{n+1} = \theta_{i,j}^{n+1} + \rho_b K_d \quad (58)$$

It is important to note that Φ^* appears in the time derivative term instead of Φ^n . The exact same solution technique used previously can be used here, except now the system of equations is linear.

Test Problems

Two test analytical problems will now be given to show the effectiveness of the solution presented. Comparison will be made with FEM results.

1-D steady-state transport

The problem consists of one-dimensional (1-D) steady-state contaminant transport over a length L in a flow of discharge velocity u , a moisture content θ , and a dispersivity D . The initial concentration C of the contaminant is 0, and then a spill occurs, giving boundary conditions of $C = 1$ at $x = 0$ and $C = 0$ at $x = L$. The governing equation is

$$D \frac{\partial^2 C}{\partial x^2} - \frac{u}{\theta} \frac{\partial C}{\partial x} = 0 \quad (59)$$

and the steady-state solution is

$$C(x) = \frac{e^{\frac{ux}{\theta D}} - e^{\frac{uL}{\theta D}}}{1 - e^{\frac{uL}{\theta D}}} \quad (60)$$

The value of the variables used are $L = 100$, $u = 0.2$, $\theta = 0.4$, $D = 50$, and $\Delta t = 10$. A grid, 11×2 , was created with a constant $\Delta x = 10$, and the problem was run on both the FV code and an LE FEM program. The FEM and FV results were essentially identical, and a plot of the analytical versus numerical results is given in Figure 28. These results are certainly acceptable. However, if u is increased, a finer or adaptive mesh is required for the same quality result.

2-D transient transport

This problem consists of saturated flow in a rectangular vertical cross section of sand of size

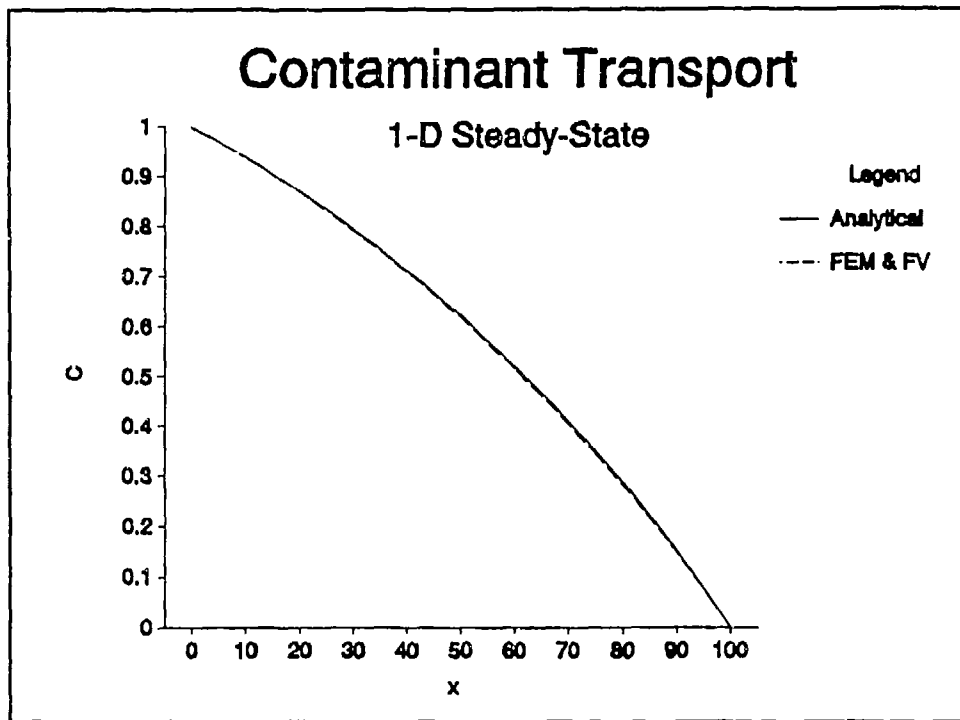


Figure 28. 1-D steady-state results

$$\begin{aligned} 0 \leq x \leq a \\ 0 \leq y \leq L \end{aligned} \quad (61)$$

that is initially clean until a spill occurs on the top of the sand ($y = L$). A concentration C_0 in a strip of length s in the middle of the top of the sand is maintained for a time t_0 , and then it decays exponentially with a decay constant α . Water is flowing in the $+x$ direction with a discharge velocity u . However, no contaminant due to dispersion flows through the boundary at $x = a$. Adsorption into the medium of bulk density ρ_b occurs linearly with a distribution coefficient of K_d .

The governing partial differential equation is

$$\left(\theta_s + \rho_b K_d\right) \frac{\partial C}{\partial t} + u \frac{\partial C}{\partial x} = \theta_s \left(D_1 \frac{\partial^2 C}{\partial x^2} + D_2 \frac{\partial^2 C}{\partial y^2} \right) \quad (62)$$

where

θ_s = maximum moisture content

D_1 = dispersion coefficient in the x direction

D_2 = dispersion coefficient in the y direction

The initial conditions are

$$C(x, y, 0) = 0 \quad (63)$$

and the boundary conditions are

$$\begin{aligned} C(0, y, t) = 0 \quad \frac{\partial C}{\partial x}(a, y, t) = 0 \quad C(x, 0, t) = 0 \\ \left[\begin{aligned} C(x, L, t) = C_0 \quad 0 \leq t \leq t_0 \\ = C_0 e^{-\alpha(t-t_0)} \quad t > t_0 \end{aligned} \right] \quad \text{for } \frac{a-s}{2} \leq x \leq \frac{a+s}{2} \quad (64) \end{aligned}$$

As part of this research, the solution to the problem was derived as

$$\begin{aligned} C(x, y, t) = \frac{8\pi D_2 C_0}{RL^2} \sum_{l=1}^{\infty} \sum_{n=1}^{\infty} \frac{\lambda_l \mu_l}{2\lambda_l \mu_l - \sin 2\lambda_l \mu_l} \\ \cdot n(-1)^{n+1} (T_1 - T_2) e^{\beta x} \sin \lambda_l x \sin \frac{n\pi}{L} y \end{aligned} \quad (65)$$

where

$$R = 1 + \frac{\rho_b K_d}{\theta_s} \quad (66)$$

and

$$\beta = \frac{u}{2\theta_s D_1} \quad (67)$$

λ_l is the l 'th solution to the equation

$$\beta \sin \lambda_l a + \lambda_l \cos \lambda_l a = 0 \quad (68)$$

Also,

$$d_l = \frac{1}{\lambda_l^2 + \beta^2} \left\{ e^{-\beta \left(\frac{a-s}{2} \right)} \left[\beta \sin \lambda_l \left(\frac{a-s}{2} \right) + \lambda_l \cos \lambda_l \left(\frac{a-s}{2} \right) \right] \right. \\ \left. - e^{-\beta \left(\frac{a+s}{2} \right)} \left[\beta \sin \lambda_l \left(\frac{a+s}{2} \right) + \lambda_l \cos \lambda_l \left(\frac{a+s}{2} \right) \right] \right\} \quad (69)$$

The two transient terms T_1 and T_2 are given by

$$T_1 = \frac{1}{\mu} (1 - e^{-\mu t}) \quad (70)$$

and

$$T_2 = \left[\frac{1}{\mu} + \frac{1}{\alpha - \mu} e^{-\alpha(t-t_0)} + \frac{\alpha}{\mu(\mu - \alpha)} e^{-\mu(t-t_0)} \right] U(t - t_0) \quad (71)$$

where

$$\mu = \frac{1}{R} \left[D_1 (\beta^2 + \lambda_l^2) + D_2 \left(\frac{n\pi}{L} \right)^2 \right] \quad (72)$$

and

$$U(t - t_0) = 0 \quad t < t_0 \\ = 1 \quad t \geq t_0 \quad (73)$$

The value of the parameters are given in Table 3. A 21 by 11 grid was used to solve the problem using both the FEM and FV codes. Figure 29 shows a comparison of analytical, FEM, and FV results for position (100, 18) for 10 time-steps where $\Delta t = 1.0$. A higher level of accuracy can be

| Table 3 Value of Parameters | | | |
|--------------------------------|------|----------|-------|
| C_0 | 1.0 | a | 100.0 |
| L | 20.0 | s | 20.0 |
| t_0 | 10.0 | α | 1.0 |
| U_a | 0.4 | ρ_b | 1.2 |
| K_d | 0.1 | u | 2.0 |
| D_1 | 50.0 | D_2 | 5.0 |

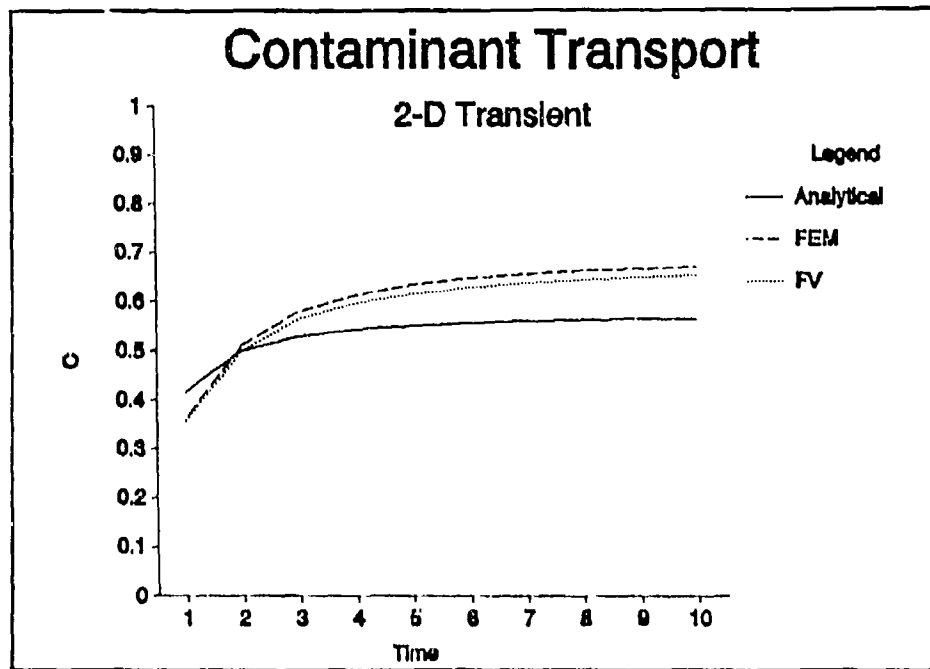


Figure 29. 2-D transient results

achieved by refining the grid near the top where the concentration is applied. However, the current grid is sufficient to show the desired comparison of results.

Scientific Visualization

Visualization of contaminant transport analysis results is an important aspect of understanding the volumes of output data. There are several techniques used, and there is potential for more research, especially with the use of translucency. One technique is to take a value of the contaminant and create the 3-D geometry representing the isolevel and perform a hidden surface plot. Another option is to cut a cross section through the plume at a particular time and plot a line or color contour of concentration on the cross section. Figure 30 shows a plume from a 3-D version of the above problem at $t = 10$. The spill now occurs on an s by s square area on the top of the $a \times b \times L$ rectangular region of porous media with, in this case, $a = b = 100$. Figure 30 contains an isolevel of $C = 0.4$, a color contour plot of concentration along the vertical cross section, $x = 50$, and a color contour plot of concentration along the vertical cross section, $y = 50$. As shown in Figure 11 for saturated flow, the surrounding porous media can be represented using translucent colors.

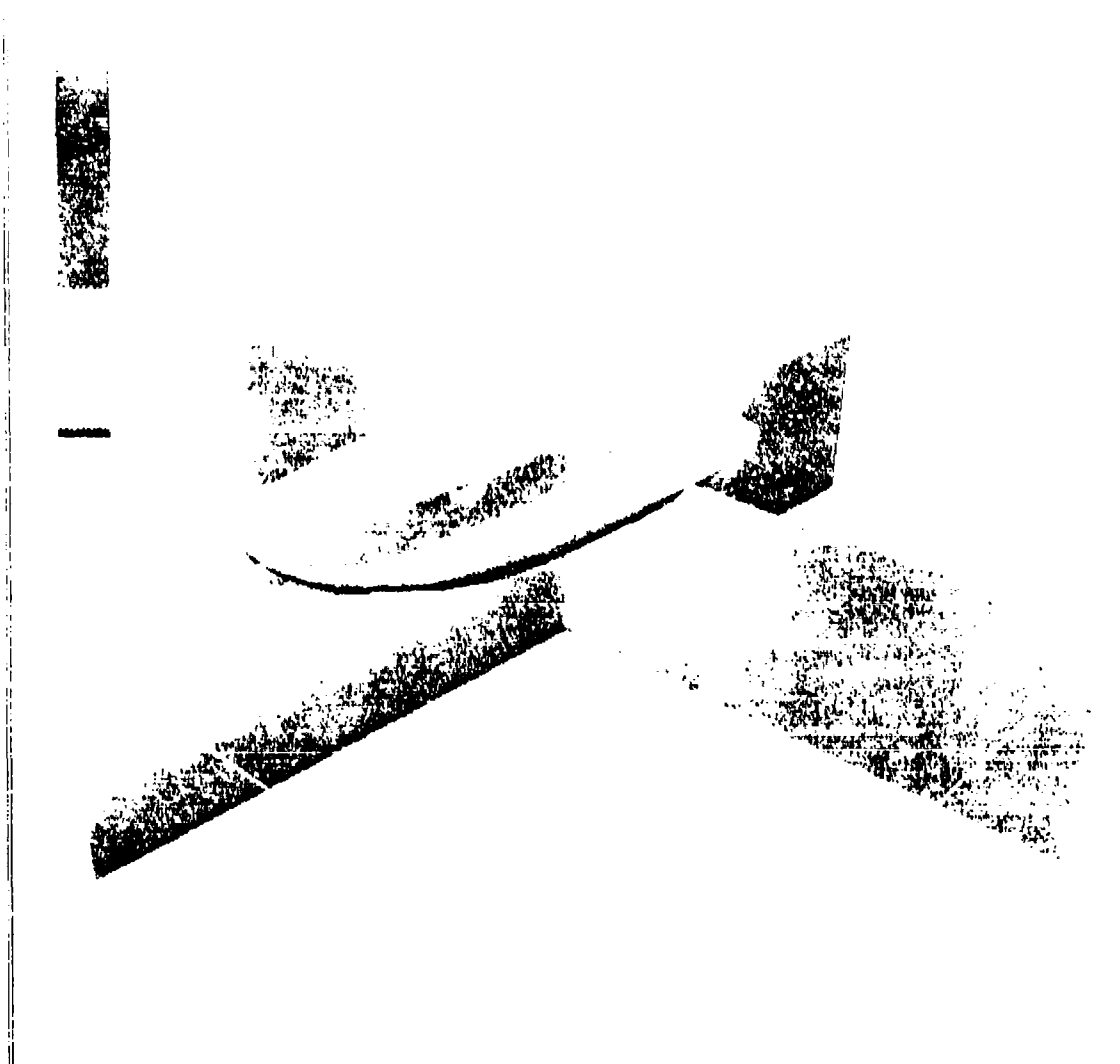


Figure 30. Isopleth and color contours

Summary and Conclusions

As in the case of unsaturated flow, there are many more problems that can be considered. There are problems with difficult geometries and heterogeneities. In some cases, the FEM will function better, and in other cases, as has been demonstrated, the FVM will function better. But it can be concluded, as before, on the basis of this study that alternative techniques such as the FVM can be a powerful tool for groundwater modeling.

References

- Anderson, E., Bai, Z., Bischof, C., Demmel, J., Dongarra, J., Du Croz, J., Greenbaum, A., Hammarling, S., McKenney, A., and Sorensen, D. (1990). "LAPACK: A portable linear algebra library for high-performance computers." *Supercomputing '90 Proceedings*. IEEE Computer Society Press, Los Alamitos, CA, 2-11.
- Cray Research, Inc. (1990). "MPGS, A distributed multi purpose graphics system, version 3.5" (computer program), Industry, Science, and Technology Dept., Eagan, MN.
- Dongarra, J., Du Croz, J., Hammarling, S., and Duff, I. (1990). "A set of level 3 basic linear algebra subprograms," *ACM Transactions of Mathematical Software* 16(1), 1-17.
- Gibbs, N. E., Poole, W. G., Jr., and Stockmeyer, P. K. (1976). "An algorithm for reducing the bandwidth and profile of a sparse matrix," *SIAM Journal of Numerical Analysis* 13(2), 235-251.
- McCormick, S. (1992). "Finite Volume Element and Multilevel Adaptive Methods." *Computational methods in water resources IX, Vol. 1: Numerical methods in water resources*. Computational Mechanics Publications, New York, 539-553.
- Putti, M. and Paniconi, C. (1992). "Evaluation of the Picard and Newton iteration schemes for three-dimensional unsaturated flow." *Computational methods in water resources IX, Vol. 1: Numerical methods in water resources*. Computational Mechanics Publications, New York, 529-536.
- Thompson, J. P., Warsi, Z. U. A., and Mastin, C. Wayne. (1985). *Numerical grid generation, foundation and applications*. Elsevier Science Publishing Co., Inc., New York, 110-111.
- Tracy, Fred T. (1991). "Application of finite element, grid generation, and scientific visualization techniques to 2-D and 3-D seepage and groundwater modeling," Technical Report ITL-91-3, U.S. Army Engineer Waterways Experiment Station, Vicksburg, MS.

- Vauclin, M., Khanji, D., and Vachaud, G. (1979). "Experimental and numerical study of a transient two-dimensional unsaturated-saturated water table recharge problem," *Water Resources Research* 15(5), 1089-1101.
- Yeh, G. T. (1990). "A Lagrangian-Eulerian method with zoomable fine-mesh approach to solving advection-dispersion equations," *Water Resources Research* 26(2), 11133-1144.
- Warner, James W. (1987). "Mathematical development of the Colorado State University finite element 2-dimensional groundwater flow model CSU-GWFLOW, version FEM2D3," Technical Report No. 2, Dept. of Civil Engineering, Colorado State University, Fort Collins, CO.

Appendix A

Derivation of Curvilinear Coordinate Equations

Purpose

The purpose of this appendix is to derive expressions used to cast partial differential equations in strong conservation form for a curvilinear coordinate system. These include the geometric conservation law, the gradient operator, and the divergence operator. 2-D versions of the equations are derived for simplicity.

Coordinate System

Each quadrilateral cell or element of a finite volume or finite element grid is transformed into a square (see Figure A1) from an (x, y) coordinate system to a curvilinear (ξ, η) coordinate system.

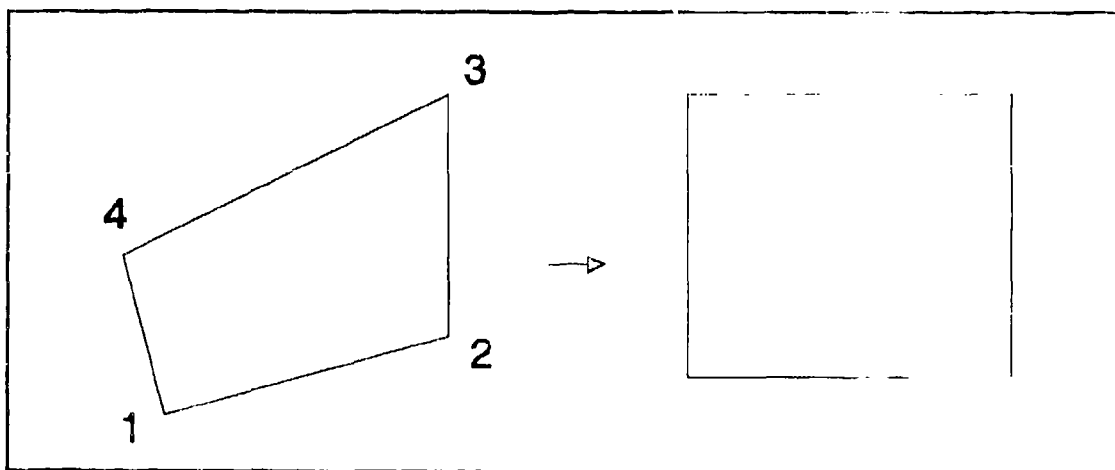


Figure A1. Transformation

Geometric Conservation Law

The geometric conservation law is a basic tool for placing equations in strong conservative form (Thompson, Warsi, and Mastin 1985).¹ A matrix oriented derivation of this equation will now be given. The chain rule of differentiation states

$$\frac{\partial f}{\partial \xi} = \frac{\partial f}{\partial x} \frac{\partial x}{\partial \xi} + \frac{\partial f}{\partial y} \frac{\partial y}{\partial \xi} \quad (\text{A1})$$

where f is a continuous function. The matrix version of this equation is

$$\begin{Bmatrix} \frac{\partial f}{\partial \xi} \\ \frac{\partial f}{\partial \eta} \end{Bmatrix} = \begin{bmatrix} \frac{\partial x}{\partial \xi} & \frac{\partial y}{\partial \xi} \\ \frac{\partial x}{\partial \eta} & \frac{\partial y}{\partial \eta} \end{bmatrix} \begin{Bmatrix} \frac{\partial f}{\partial x} \\ \frac{\partial f}{\partial y} \end{Bmatrix} \quad (\text{A2})$$

An alternate way is

$$\begin{Bmatrix} \frac{\partial f}{\partial x} \\ \frac{\partial f}{\partial y} \end{Bmatrix} = \begin{bmatrix} \frac{\partial \xi}{\partial x} & \frac{\partial \eta}{\partial x} \\ \frac{\partial \xi}{\partial y} & \frac{\partial \eta}{\partial y} \end{bmatrix} \begin{Bmatrix} \frac{\partial f}{\partial \xi} \\ \frac{\partial f}{\partial \eta} \end{Bmatrix} \quad (\text{A3})$$

Let the determinant of the matrix in Equation A2 be defined by

$$J = \frac{\partial x}{\partial \xi} \frac{\partial y}{\partial \eta} - \frac{\partial x}{\partial \eta} \frac{\partial y}{\partial \xi} \quad (\text{A4})$$

The inverse of the matrix in Equation A2 can also be multiplied to both sides of Equation A2 to produce

$$\begin{Bmatrix} \frac{\partial f}{\partial x} \\ \frac{\partial f}{\partial y} \end{Bmatrix} = \frac{1}{J} \begin{bmatrix} \frac{\partial y}{\partial \eta} & -\frac{\partial y}{\partial \xi} \\ -\frac{\partial x}{\partial \eta} & \frac{\partial x}{\partial \xi} \end{bmatrix} \begin{Bmatrix} \frac{\partial f}{\partial \xi} \\ \frac{\partial f}{\partial \eta} \end{Bmatrix} \quad (\text{A5})$$

Comparing Equations A3 and A5 gives

$$\nabla \xi = \begin{Bmatrix} \frac{\partial \xi}{\partial x} \\ \frac{\partial \xi}{\partial y} \end{Bmatrix} = \frac{1}{J} \begin{Bmatrix} \frac{\partial y}{\partial \eta} \\ -\frac{\partial x}{\partial \eta} \end{Bmatrix} \quad (\text{A6})$$

¹ References cited in this appendix are listed following the main text.

and

$$\nabla\eta = \begin{Bmatrix} \frac{\partial\eta}{\partial x} \\ \frac{\partial\eta}{\partial y} \end{Bmatrix} = \frac{1}{J} \begin{Bmatrix} -\frac{\partial y}{\partial\xi} \\ \frac{\partial x}{\partial\xi} \end{Bmatrix} \quad (\text{A7})$$

Equations A6 and A7 can now be used to evaluate

$$\frac{\partial(J\nabla\xi)}{\partial\xi} + \frac{\partial(J\nabla\eta)}{\partial\eta} = \begin{Bmatrix} \frac{\partial^2 y}{\partial\xi\partial\eta} \\ -\frac{\partial^2 x}{\partial\xi\partial\eta} \end{Bmatrix} + \begin{Bmatrix} -\frac{\partial^2 y}{\partial\xi\partial\eta} \\ \frac{\partial^2 x}{\partial\xi\partial\eta} \end{Bmatrix} \quad (\text{A8})$$

It is clear now that

$$\frac{\partial(J\nabla\xi)}{\partial\xi} + \frac{\partial(J\nabla\eta)}{\partial\eta} = 0 \quad (\text{A9})$$

which is the geometric conservation law.

Gradient

The gradient of f from Equation A3 is

$$\nabla f = \nabla\xi \frac{\partial f}{\partial\xi} + \nabla\eta \frac{\partial f}{\partial\eta} \quad (\text{A10})$$

Multiplying Equation A10 by J and Equation A9 by f and adding gives

$$J\nabla f = J\nabla\xi \frac{\partial f}{\partial\xi} + J\nabla\eta \frac{\partial f}{\partial\eta} + \frac{\partial(J\nabla\xi)}{\partial\xi} f + \frac{\partial(J\nabla\eta)}{\partial\eta} f \quad (\text{A11})$$

Combining terms gives the desired result

$$J\nabla f = \frac{\partial(Jf\nabla\xi)}{\partial\xi} + \frac{\partial(Jf\nabla\eta)}{\partial\eta} \quad (\text{A12})$$

Divergence

The divergence of a vector

$$\{F\} = \begin{Bmatrix} f_x \\ f_y \end{Bmatrix} \quad (\text{A13})$$

in matrix notation becomes

$$\nabla^T \{F\} = \frac{\partial f_x}{\partial x} + \frac{\partial f_y}{\partial y} \quad (A14)$$

Now if Equation A12 is modified to the form of an operator, this yields

$$\mathcal{J}\nabla \circ = \frac{\partial}{\partial \xi} (\mathcal{J}\nabla \xi \circ) + \frac{\partial}{\partial \eta} (\mathcal{J}\nabla \eta \circ) \quad (A15)$$

Taking the transpose of Equation A15 and operating on $\{F\}$ gives

$$\mathcal{J}\nabla^T \{F\} = \frac{\partial}{\partial \xi} (\mathcal{J}\nabla \xi^T \{F\}) + \frac{\partial}{\partial \eta} (\mathcal{J}\nabla \eta^T \{F\}) \quad (A16)$$

which is the desired result for the divergence.

| REPORT DOCUMENTATION PAGE | | | Form Approved OMB No. 0704-0188 | |
|---|---|--|------------------------------------|--|
| <small>Public reporting burden for this collection of information is estimated to average 1 hour per response, including the time for reviewing instructions, searching existing data sources, gathering and maintaining the data needed, and completing and reviewing the collection of information. Send comments regarding this burden estimate or any other aspect of this collection of information, including suggestions for reducing this burden, to Washington Headquarters Services, Directorate for Information Operations and Reports, 1215 Jefferson Davis Highway, Suite 1204, Arlington, VA 22202-4302, and to the Office of Management and Budget, Paperwork Reduction Project (0704-0188), Washington, DC 20503.</small> | | | | |
| 1. AGENCY USE ONLY (Leave blank) | 2. REPORT DATE September 1994 | 3. REPORT TYPE AND DATES COVERED Final report | | |
| 4. TITLE AND SUBTITLE Application of Computational and Visualization Methods to Groundwater Modeling | | 5. FUNDING NUMBERS | | |
| 6. AUTHOR(S) Fred T. Tracy | | | | |
| 7. PERFORMING ORGANIZATION NAME(S) AND ADDRESS(ES) U.S. Army Engineer Waterways Experiment Station 3909 Halls Ferry Road, Vicksburg, MS 39180-6199 | | 8. PERFORMING ORGANIZATION REPORT NUMBER Technical Report ITL-94-7 | | |
| 9. SPONSORING/MONITORING AGENCY NAME(S) AND ADDRESS(ES) Assistant Secretary of the Army (R&D) Washington, DC 20315 | | 10. SPONSORING/MONITORING AGENCY REPORT NUMBER | | |
| 11. SUPPLEMENTARY NOTES Available from National Technical Information Service, 5285 Port Royal Road, Springfield, VA 22161. | | | | |
| 12a. DISTRIBUTION / AVAILABILITY STATEMENT Approved for public release; distribution is unlimited. | | 12b. DISTRIBUTION CODE | | |
| 13. ABSTRACT (Maximum 200 words) This report documents basic and applied research in the area of groundwater modeling. A three-dimensional finite element method program and model for the real-world problem of flow near Rocky Mountain Arsenal (RMA) is described, and a comparison with a two-dimensional finite element method RMA computation is done to help determine when a three-dimensional analysis is needed. Scientific visualization techniques and Cray Y-MP improvements developed in this RMA study are described. The finite volume method is applied to saturated/unsaturated flow and contaminant transport, and the results are compared to finite element method solutions. Nonlinear Newton iteration for unsaturated flow and the Lagrangian-Eulerian method for contaminant transport are discussed. Experimental results and analytical solutions are used to compare different procedures. Finally, contaminant transport results are viewed using scientific visualization tools. | | | | |
| 14. SUBJECT TERMS Containment transport Groundwater modeling Finite element method Scientific visualization Finite volume method Unsaturated flow | | | 15. NUMBER OF PAGES 68 | |
| | | | 16. PRICE CODE | |
| 17. SECURITY CLASSIFICATION OF REPORT UNCLASSIFIED | 18. SECURITY CLASSIFICATION OF THIS PAGE UNCLASSIFIED | 19. SECURITY CLASSIFICATION OF ABSTRACT | 20. LIMITATION OF ABSTRACT | |